Earthquake response control effects of coupled structural systems incorporating a negative stiffness connector: Experimental and numerical investigation

Sonia Longjam , Kazutaka Shirai [1,*]

Faculty of Engineering, Hokkaido University, Sapporo, Japan

ABSTRACT

Coupled vibration control (CVC) systems, which typically consist of two frames and connectors, such as stiffness and damping elements, can be used for the seismic protection of coupled or adjacent structures. This study aims to experimentally and numerically elucidate the response behavior and control effects of CVC structural systems comprising a mainframe and subframe incorporating passive negative stiffness (PNS) at the connection subjected to earthquakes. Shake table experiments were conducted using CVC system specimens incorporating a PNS device (PNSD) consisting of curved-leaf springs under dynamic excitations. A significant seismic response reduction for the mainframe of the CVC specimen under simulated waves was achieved by incorporating the PNSD at the connection. Moreover, a response simulation was performed using six-story CVC structure models connected by negative stiffness and viscous damping elements subjected to simulated and observed seismic wave inputs. The displacement and acceleration peak response of the mainframe using the numerical CVC models was lower than that of the uncontrolled model. Therefore, incorporating negative stiffness and viscous damping connectors into CVC systems can reduce the seismic response. This study contributes to the advancement of aseismic technologies for coupled or adjacent buildings utilizing the PNS.

1. Introduction

Coupled vibration control (CVC) structural systems typically consist of two frames and connectors, such as stiffness and damping elements. CVC systems with a proper connecting mechanism that depends on the structural properties of the two frames can be a solution for protecting coupled or adjacent structures against earthquakes [1–17]. To date, various CVC structures incorporating various connecting devices, including steel hysteresis dampers [3,4], fluid dampers [1,14], magnetorheological (MR) dampers [7,10,11,12], tuned mass damper inerters [13,17], viscous inertial mass dampers [15], and friction dampers [16], have been proposed and investigated to mitigate the response when subjected to seismic input motions. Passive [2,3,4,6,16], semi-active [7,10,11,12], and active [5,8] control methods for CVC systems have been studied theoretically, numerically, and experimentally, and the results have proved a potential effectiveness for the seismic protection of buildings. However, employing only zero or positive stiffness at the connectors of CVC systems to achieve an optimal tuning and obtain a better control performance may be difficult depending on the properties of the two frames [18].

In contrast to positive stiffness, negative stiffness generally generates a decreased (negative) restoration force as the displacement increases.

The use of negative stiffness can be considered a potential response control strategy for buildings against dynamic disturbances, such as earthquakes. During the last few decades, many studies have been conducted to explore negative stiffness devices (NSDs) and structural systems containing NSDs [19–23]. Iemura et al. [19] used the self-weight of the structure and developed a negative-stiffness damper based on a slide bearing with a convex curve. Nagarajaiah et al. [20] and Sarlis et al. [21] studied a passive NSD based on a vertical preloaded coil spring placed between two chevron braces and a horizontal-gap spring assembly. Wang et al. [22] investigated a structural system with a negative-stiffness amplifying damper consisting of a passive NSD [20,21], positive-stiffness spring, and dashpot. Shirai et al. [23] proposed another passive NSD comprising curved-leaf springs. This passive NSD exhibited an initial negative stiffness created by the pre-compressed strain energy stored in the curved-leaf springs, followed by an increased second negative stiffness with the occurrence of snap-through buckling. However, these previous studies on NSDs explored the seismic response of individual, that is, nonadjacent or noncoupled, structural systems with NSDs.

Few studies have been conducted on CVC structural systems connected by negative stiffness. Yamada et al. [24], Ikawa et al. [25], and Shimizu and Kurino [26,27] explored coupled structures linked by

negative or pseudo-negative stiffness using active or semi-active controls subjected to earthquakes. Longjam and Shirai [18,28] analytically and numerically investigated a coupled system formed by connecting two single-degree-of-freedom (SDOF) systems with negative stiffness. These studies [18,24–28] showed the potential effectiveness of CVC systems connected by negative stiffness. However, the response characteristics and control performance of passive NSDs as connecting elements for CVC systems subjected to earthquakes have not been fully clarified. Moreover, there have been no experimental studies on seismic response control of CVC systems incorporating the passive NSD comprising curved-leaf springs as the connector.

This study aims to experimentally and numerically elucidate the response behavior and control effects of CVC structural systems comprising a mainframe and subframe incorporating passive negative stiffness (PNS) at the connection subjected to earthquakes. Shaking table experiments were conducted using CVC system specimens consisting of an SDOF mainframe and SDOF subframe, which were connected by PNS devices (PNSDs) consisting of leaf springs. The dynamic responses under simulated earthquake motions and sinusoidal waves were obtained using experiments, and the response reduction effectiveness of PNSDs was investigated. In addition, a response analysis was conducted using six degrees-of-freedom (6DOF) CVC building models connected by PNS and damping elements to evaluate the response reduction effects when subjected to seismic motions. This study is an expansion of a previous work [29] that presents new experimental and numerical data and findings. This study contributes to the advancement of seismic protection technologies for building structures utilizing the PNS in adjacent structural systems.

2. Shake table experiments

2.1. Theoretical foundation and specimen overview of experiments

Kageyama et al. [2] derived a theoretical formula for optimal tuning and damping conditions for a CVC system with spring and viscous damping connectors. The theoretical formula of the optimal connection stiffness that minimizes the peak amplitude of the displacement transfer function for the mainframe can be expressed as:

$$K_{0,\text{opt}} = \frac{(\alpha - \mu)(-2 - \mu + \alpha\mu)}{2(1 + \alpha)(1 + \mu)^2}K_1 \tag{1}$$

where, $K_{0,\text{opt}}$ is the optimal connection stiffness, K_1 is the stiffness of the SDOF mainframe, α is the stiffness ratio of the SDOF subframe to the SDOF mainframe, and μ is the mass ratio of the SDOF subframe to the SDOF mainframe.

Also, Longjam and Shirai [18] showed a calculation result of the optimal connecting stiffness for various parameter combinations that require negative stiffness at the connecting portion. For example, in the case of $\mu = 0.5$ and $\alpha = 1.0$, a negative connection stiffness (i.e., $K_{0,\text{opt}} = -0.1111 K_1$) is required. Based on the above foundation, in the present shake table experiments, a target parameter combination of $\mu = 0.5$ and $\alpha = 1.0$ that requires negative stiffness at the connector was adopted in the basic design of the specimens.

The shake table experiments were conducted using CVC system specimens with PNSDs. The specimen comprised a mainframe system and subframe system, which were connected by a PNSD, representing a simplified model for CVC building structures with a PNS element as the connector. Three controlled cases (CVC-1, CVC-2, and CVC-3) with different PNSDs (PNSD-1, PNSD-2, and PNSD-3) connecting the mainframe and subframe were examined. In addition, three uncontrolled cases were examined for comparison purposes; the first case had the mainframe alone (SDOF-MF), the second case had the subframe alone (SDOF-SF), whereas in the last case the mainframe and subframe were almost rigidly connected (CVC-R).

2.2. Methods of experiments

2.2.1. Coupled vibration control specimens and shake table

Figs. 1 and 2 show the CVC system specimen with PNSD. A unidirectional shake table (maximum payload: 1000 N; maximum displacement: 100 mm; maximum acceleration: 1.0 G) was used in the experiments. The excitation direction of the shake table was in the X-direction. Each of the mainframe and subframe of the specimen was supported by a bearing (linear guide) in the X-direction placed on the shake table, connected by restoring members with positive stiffness to the shake table, and allowed to move in the X-direction; thus, it was behaving as an SDOF vibration system. The masses of the moving portions for the mainframe, M_{MF}, and subframe, M_{SF}, were 0.945 and 0.468 kg, respectively. Thus, the mass ratio of the subframe to the mainframe was $\mu = M_{\text{SF}}/M_{\text{MF}} = 0.5$. The mainframe and subframe were provided with a positive stiffness by connecting the tension coil springs in series and parallel. These coil springs functioned as positive stiffness restoring members without becoming loose in both the positive and negative sides in the X-direction because an initial tensile deflection was applied to them. After each excitation, the mainframe and subframe of the specimen were restored to neutral positions to remove residual displacements, and then the next excitation was performed.

2.2.2. PNSDs

In contrast to the positive stiffness produced by general springs with an increasing displacement, negative stiffness provides a negative restoring force that further increases the displacement. Shirai et al. [23] proposed a PNSD using curved-leaf springs. In addition, they examined the response behavior of an SDOF system incorporating a PNSD [23]. This study adopted PNSDs using curved-leaf springs, which were based on a PNSD presented in [23] with dimensional modifications. Unlike the previous study [23], PNSDs were used as the connecting element of the CVC structural system. Fig. 3 illustrates a conceptual diagram of the PNSD connector between the mainframe and subframe. The Y-directional spacing between the mainframe and subframe was maintained constant, and the two curved-leaf springs of the PNSD were precompressed at the neutral position, as shown in Fig. 3(a). The dotted regions in Fig. 3(a) indicate the positions of the leaf springs, where snap-through buckling occurs, depending on the drift between the mainframe and subframe in the X-direction. When snap-through buckling occurs, forces are applied to the mainframe and subframe in a direction that further increases (or decreases) the drift between the mainframe and subframe, as shown in Fig. 3(b) and (c). Owing to the effects of geometric nonlinearity, PNSD can exert a negative restoring force, that is, negative stiffness.

In the experiments, three PNSDs (PNSD-1, PNSD-2, and PNSD-3) were used and incorporated into CVC-1, CVC-2, and CVC-3. Table 1 lists the specifications of the PNSDs. Fig. 4 shows the production drawings of the PNSDs before the bending process. The curved-leaf springs used in each PNSD comprised two outside plates and one inside plate. The ends of the two outside plates were bent and bolted to the center of the inside plate such that leaf springs were built to attain an initial curvature. Two identical curved-leaf springs were prepared and placed bilaterally symmetrically for each PNSD. The material of the plate of the PNSDs was stainless steel SUS304. The masses of the plates of the curved-leaf spring portion (including the bolts at the center) for the PNSDs were 0.0036, 0.0056, and 0.0093 kg for PNSD-1, PNSD-2, and PNSD-3, respectively. Fig. 5(a)–(c) depicts photographs of PNSD-1, PNSD-2, and PNSD-3 incorporated between the mainframe and subframe. The inner span for each PNSD between the rigid beams of the mainframe and subframe was maintained constant at 146 mm in the Y-direction during the experiments. Thus, the curved-leaf springs of the PNSD were subjected to pre-compression in the Y-direction at the neutral displacement position. The initial and second stiffnesses for each PNSD were evaluated based on the results from sinusoidal wave input (frequency: 1.0 Hz, displacement amplitudes: 10–18 mm) when the
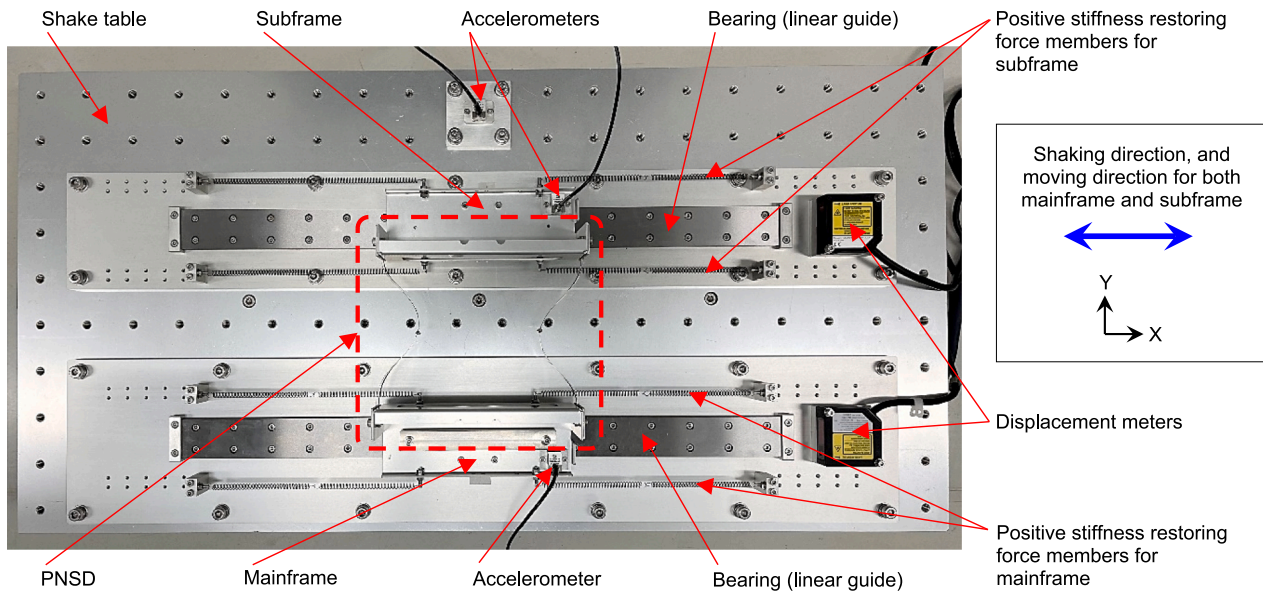
Fig. 1. Photograph of the plan view of a coupled vibration control (CVC) system specimen connected by a passive negative stiffness device (PNSD) mounted on a shake table.
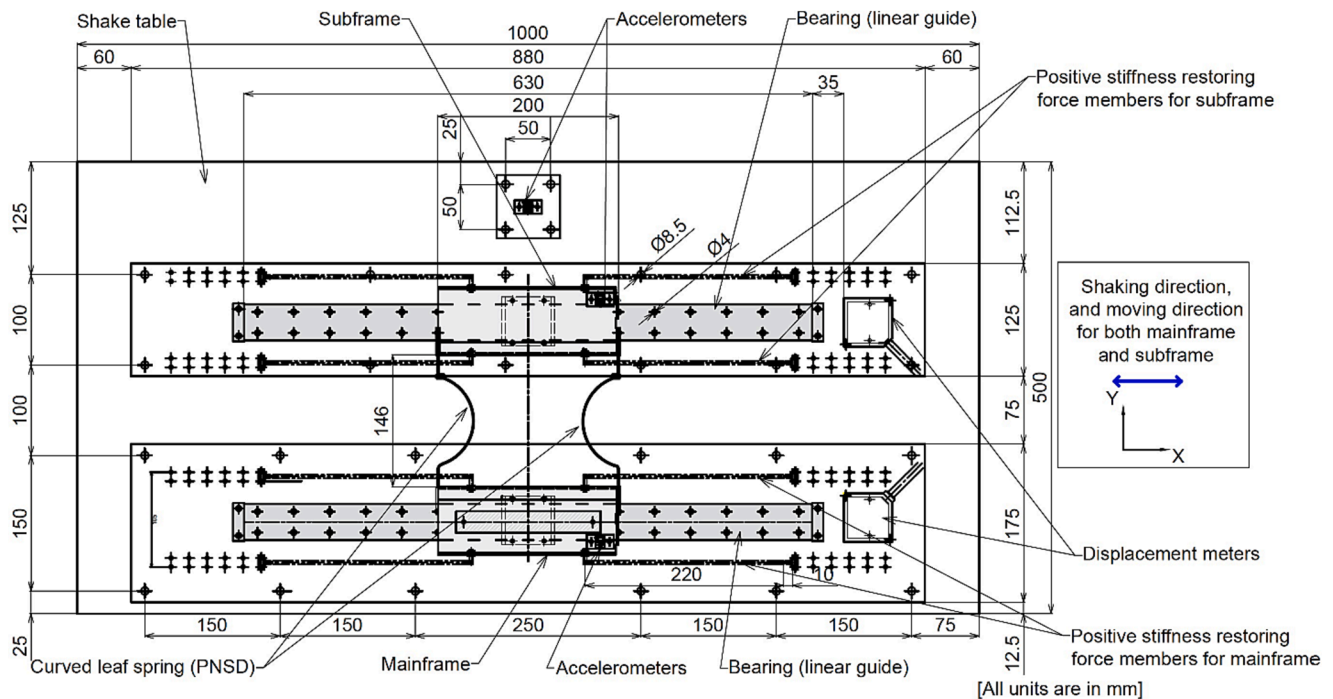

Fig. 2. Plan drawing of the CVC system specimen, PNSD, and shake table.

subframe (fixed to the shake table) and the mainframe were connected by the PNSD. The input displacement amplitudes of 10–18 mm were determined such that the range of response displacements included those before and after the onset of snap-through buckling of each PNSD. Fig. 5(d) shows the case when the mainframe and subframe were rigidly connected for comparison purposes.

In the experiments, basically, both the mainframe and subframe were not fixed to the shake table and were allowed to move in the X-direction. The results of this configuration are described in Subsection 2.3 excluding Subsection 2.3.2(b) and (c). However, as aforementioned, when evaluating the initial and second stiffnesses of the PNSDs, each PNSD was installed between the mainframe and subframe, the subframe

was fixed to the shake table, and only the mainframe was allowed to move. The results of this configuration are presented in Subsection 2.3.2 (b) and (c).

2.2.3. Instrumentation

In the experiments, the relative displacements from the shake table of the mainframe and subframe of the specimen were measured using two laser displacement meters attached to the shake table. The absolute accelerations for the shake table and the mainframe and subframe of the specimen were measured using strain gauge-type accelerometers with mass of 0.025 kg (excluding cable) and response frequency of DC–60 Hz or DC–100 Hz. The data-sampling frequency was 0.2 kHz. The obtained
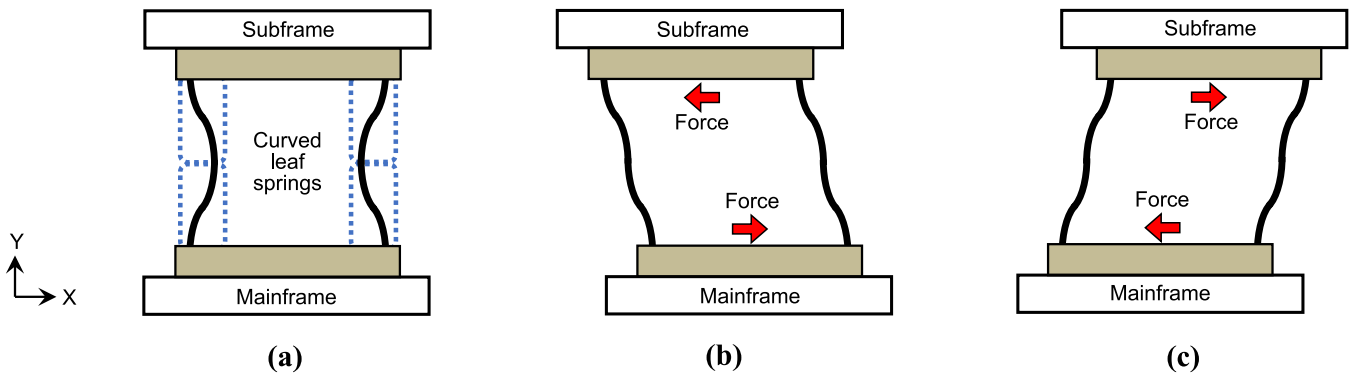
Fig. 3. Schematic of the PNSD: **(a)** at the neutral position; **(b)** at a deformed position (negative side); and **(c)** at a deformed position (positive side).

Table 1
Specification of the passive negative stiffness devices (PNSDs) used in the experiments.

Device name	Plate thickness (mm)	Plate width (mm)	Plate length (before bending) (mm)	Inner span of device (when installed) (mm)
PNSD-1	0.2	3.5	174	146
PNSD-2	0.2	5.0	174	146
PNSD-3	0.1	14.0	174	146

acceleration and displacement data were smoothed using a moving average (rectangular window: 0.035 s).

2.2.4. Input motions used in the experiments

In the experiments, sinusoidal and simulated earthquake waves were used as input motions. The sinusoidal waves had three different frequencies, 1.0, 1.5, and 1.2 Hz, which roughly corresponded to the natural frequencies of SDOF-MF, SDOF-SF, and CVC-R, respectively. Each sinusoidal wave was composed of a five-cycle sine function for the steady portion, with displacement amplitudes in the range of 10–18 mm. Five waves, namely Waves S1–5, were adopted for the simulated earthquakes. For each simulated wave, input magnifications of 0.2, 0.3,

0.4, 0.45, and 0.5 were used. Fig. 6(a) and (b) displays the time-history acceleration waveforms of the sinusoidal wave (frequency: 1.0 Hz, amplitude: 10 mm) and the simulated wave (Wave S5, input magnification: 0.45). The velocity response spectra for the five simulated waves (Waves S1–5, damping ratio: 0.05, input magnification: 0.45) are shown in Fig. 6(c).

2.2.5. Free vibration measurement methods

Free vibration measurements for the SDOF-MF, SDOF-SF, and CVC-R specimens were performed prior to the shake table experiments to ascertain their natural frequencies and damping ratios. Each specimen (SDOF-MF, SDOF-SF, and CVC-R) was individually subjected to free vibrations without employing PNSDs, that is, with only restoring members having positive stiffness. By releasing the mainframe (or subframe) after providing an initial displacement of 40 mm in the vibrating direction (X-direction), a free vibration was generated. The natural frequencies and damping ratios of the specimens were calculated based on the displacement time-history waveforms obtained from the free vibration measurements. The natural frequencies were computed using the time interval between the wave peak amplitudes. The damping ratios were determined using the logarithmic damping rate derived from the peak amplitude ratios of the waveforms.
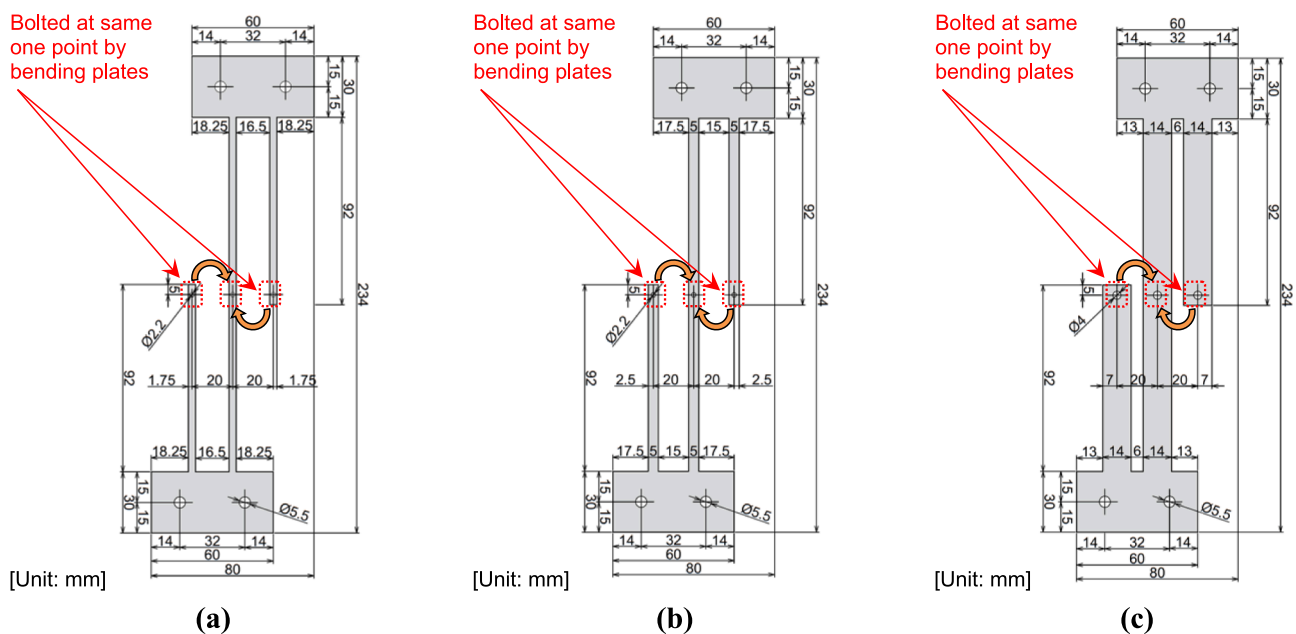

Fig. 4. Production drawings of the PNSDs (before the bending process) used in the experiments: **(a)** PNSD-1 (plate thickness: 0.2 mm); **(b)** PNSD-2 (plate thickness: 0.2 mm); and **(c)** PNSD-3 (plate thickness: 0.1 mm).
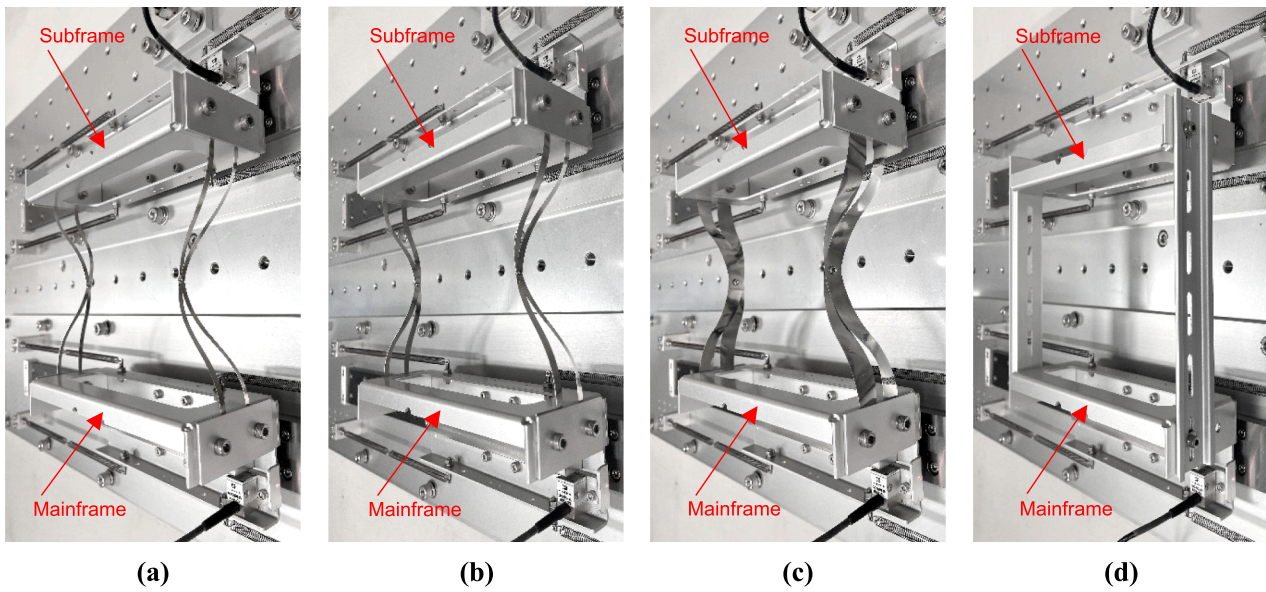
Fig. 5. Photographs of the side views of PNSDs installed between the mainframe and subframe of the specimen: **(a)** PNSD-1 (CVC-1); **(b)** PNSD-2 (CVC-2); **(c)** PNSD-3 (CVC-3); and **(d)** rigid connection (CVC-R).
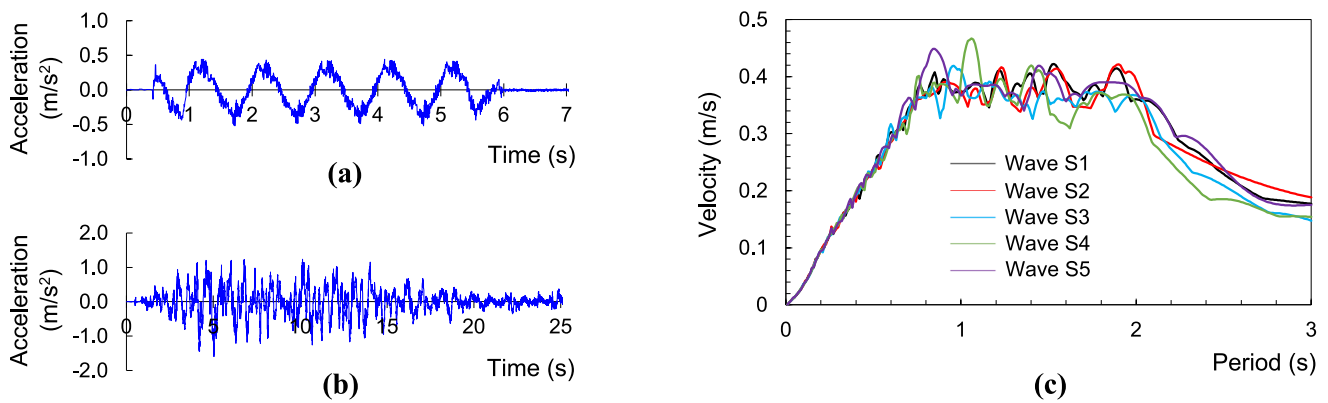

Fig. 6. Input motions used in the experiments: **(a)** time-history acceleration of the sinusoidal wave (frequency: 1.0 Hz, amplitude: 10 mm); **(b)** time-history acceleration of Wave S5 (input magnification: 0.45); and **(c)** velocity response spectra of Waves S1–5 (input magnification: 0.45, damping ratio: 0.05).

2.3. Experimental results

2.3.1. Free vibration measurement results

Table 2 lists the natural period and damping ratio for the SDOF-MF, SDOF-SF, and CVC-R specimens obtained using the free vibration measurements. Therefore, frequencies of the sinusoidal waves used in the shake table experiments, as presented in Subsection 2.2.4, were determined. The relatively high damping ratio observed from the free vibration measurements was attributed to the resistance forces by the bearings (linear guides). The resistance forces by the bearings functioned to exert an approximately bilinear shape restoring force

Table 2
Natural frequencies and damping ratios of specimens obtained from free vibration measurements.

Specimen name	Natural period (s)	Natural frequency (Hz)	Damping ratio
SDOF-MF	0.953	1.05	0.15
SDOF-SF	0.689	1.45	0.13
CVC-R (Mainframe)	0.833	1.20	0.17
CVC-R (Subframe)	0.832	1.20	0.17

characteristic for the mainframe and subframe (Subsection 2.3.2). The resistance forces by the bearings were common to all specimens (SDOF-MF, SDOF-SF, CVC-1, CVC-2, CVC-3, and CVC-R) because the linear guides used for each specimen were identical.

2.3.2. Results under sinusoidal wave inputs

(a) Response without the PNSD.

Fig. 7 depicts the response time-history acceleration of SDOF-MF and SDOF-SF, that is, the mainframe and subframe without PNSDs, under the sinusoidal waves (input displacement amplitude: 10 mm) at frequencies of 1.0 and 1.5 Hz, respectively. A gradually amplifying response occurred due to the resonance until approximately 6 and 5 s for the mainframe and subframe, respectively; subsequently, a damped free vibration response was observed.

Fig. 8 depicts the response inertial force and displacement relationships for SDOF-MF and SDOF-SF under the sinusoidal wave inputs. The inertial force was calculated using the response acceleration and mass. A bilinear-shape hysteresis loop was observed because of the resistance of the linear guides and positive stiffness restoring force members. In addition, Fig. 8 includes a linear function computed using the least-squares method along with the decision coefficient R^2. Stiffnesses of the positive stiffness restoring members for SDOF-MF and SDOF-SF were
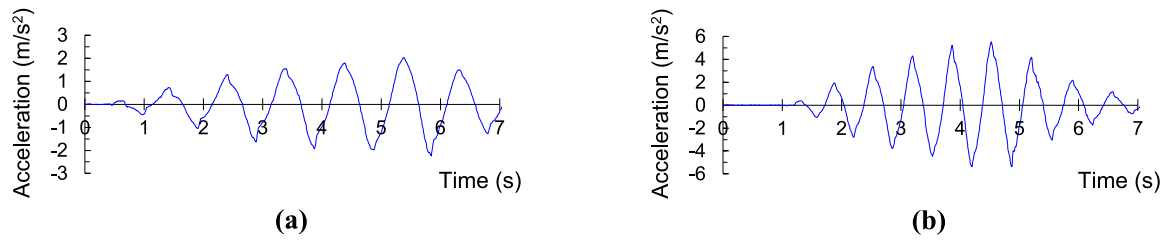
Fig. 7. Time-history acceleration response under the sinusoidal wave (input amplitude: 10 mm) obtained from the experiments: **(a)** SDOF-MF (input frequency: 1.0 Hz); and **(b)** SDOF-SF (input frequency: 1.5 Hz).
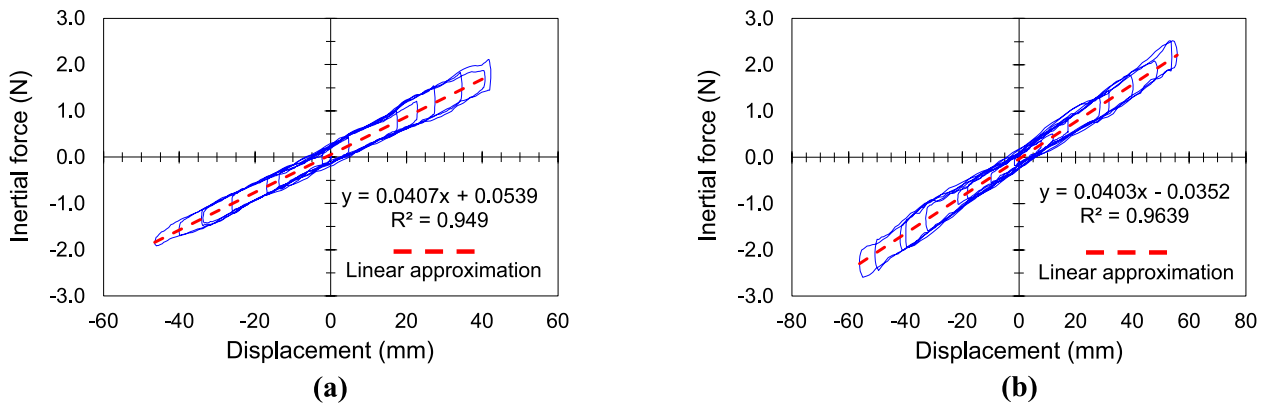

Fig. 8. Response hysteresis loop under the sinusoidal wave (input amplitude: 10 mm) obtained from the experiments along with a linear approximation: **(a)** SDOF-MF (input frequency: 1.0 Hz); and **(b)** SDOF-SF (input frequency: 1.5 Hz).

determined to be $K_{MF} = 0.0407$ and $K_{SF} = 0.0403$ N/mm, respectively. Thus, the stiffness ratio $\alpha = K_{SF}/K_{MF}$ of the specimens in these experiments was confirmed as $\alpha = 1.0$. Moreover, the natural frequencies of SDOF-MF and SDOF-SF (without the PNSDs) were calculated to be 1.0 and 1.5 Hz, respectively, using the stiffnesses and masses. This result roughly agrees with the values obtained from the free vibration measurements presented in Table 2. The maximum section force (intercept) of the inertial force at the neutral displacement was approximately 0.24 and 0.31 N for SDOF-MF and SDOF-SF, respectively, and these section forces were attributed to the resistance by the linear guides.

(b) Evaluation of initial and second stiffnesses of the PNSDs.

The initial and second stiffnesses of the PNSDs were investigated by setting each device (PNSD-1, PNSD-2, and PNSD-3) between the mainframe and subframe, where the subframe was fixed to the shake table and only the mainframe was allowed to move along the linear guide. The investigation used sinusoidal wave inputs with amplitudes in the range of 10–18 mm and a frequency of 1.0 Hz. Fig. 9 depicts the obtained

response inertial force and displacement relationship of the vibrating system with PNSD-1. Moreover, to evaluate the contribution of PNSD-1, the subtracted force was calculated by subtracting the positive restoring force of the mainframe, that is, K_{MF} times the displacement of the mainframe, from the inertial force, that is, the inertial force in Fig. 9.

Fig. 10 shows the subtracted hysteresis loops obtained for PNSD-1. As shown in Fig. 10, a roughly constant negative stiffness was observed over a displacement range of ± 10 mm. As mentioned in Section 1, the previous study [23] reported that the passive NSD with curved-leaf springs exhibited an initial negative stiffness created by the pre-compressed strain energy stored in the curved-leaf springs, followed by an increased second negative stiffness with the occurrence of snap-through buckling. Considering this, it is inferred that the initial negative stiffness within a displacement of ± 10 mm for PNSD-1 in the present experiments was owing to a pre-compression at the installation applied to the leaf springs. Moreover, an increased negative stiffness was generated by PNSD-1 at displacements of + 45 to + 51 mm. This
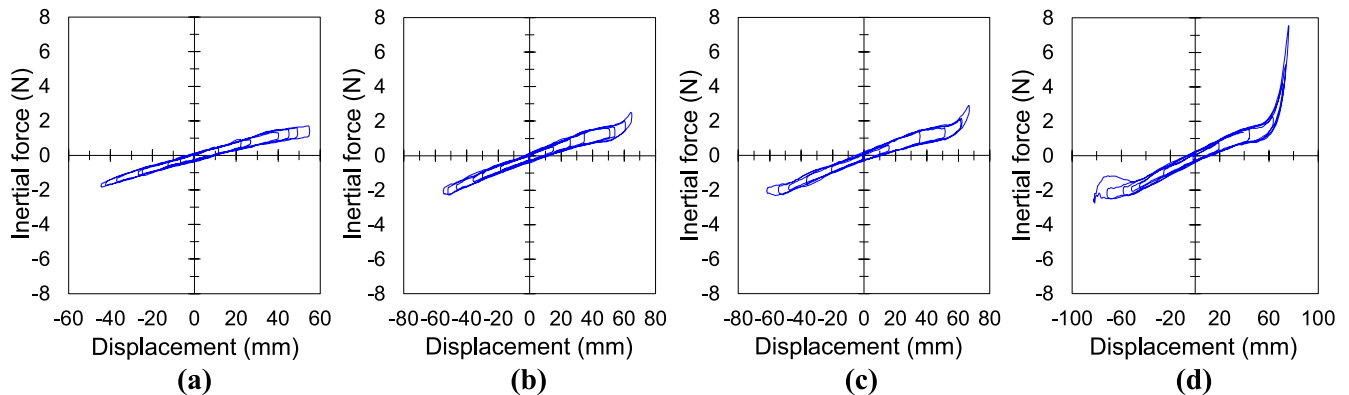

Fig. 9. Response hysteresis loops of the vibrating system (the mainframe with PNSD-1 and fixed-subframe) under the sinusoidal waves (frequency: 1.0 Hz) obtained from the experiments: **(a)** input amplitude: 10 mm; **(b)** input amplitude: 12 mm; **(c)** input amplitude: 13 mm; and **(d)** input amplitude: 15 mm.
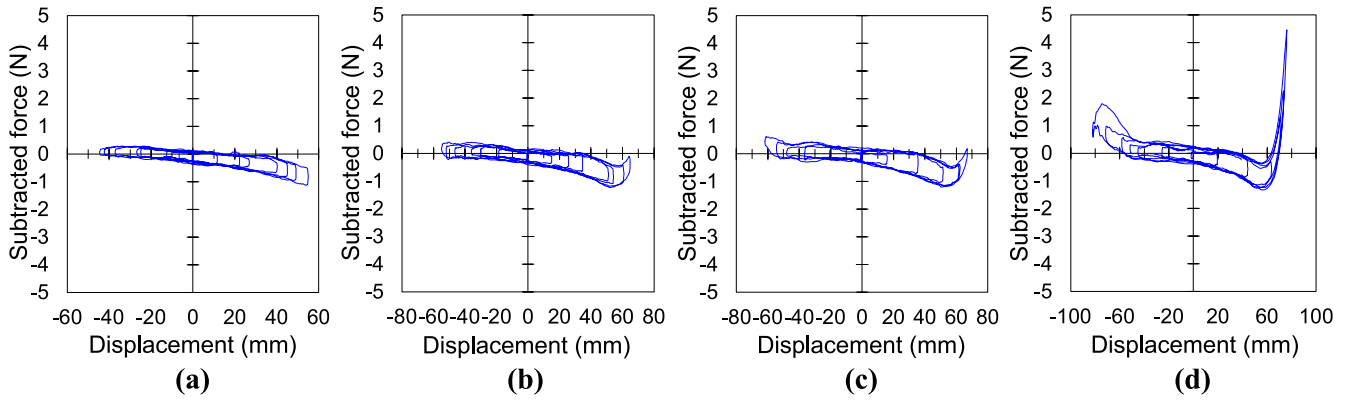
Fig. 10. Subtracted hysteresis loops for PNSD-1 under the sinusoidal waves (frequency: 1.0 Hz) obtained from the experiments: **(a)** input amplitude: 10 mm; **(b)** input amplitude: 12 mm; **(c)** input amplitude: 13 mm; and **(d)** input amplitude: 15 mm.

increased negative stiffness may have resulted from snap-through buckling of the leaf springs of PNSD-1. Beyond a displacement of approximately + 58 mm, the negative stiffness reversed to a positive stiffness because of the tensile brace act of the leaf springs when the displacement reached their deformation limit of the leaf springs.

The initial stiffness for the vibrating system was calculated using the least-squares approximation from the inertial force–displacement data within a displacement of ± 10 mm, as shown in Fig. 9. The initial stiffnesses of the vibrating system were obtained as 0.0352, 0.0355, 0.0357, and 0.037 N/mm for input amplitudes of 10, 12, 13, and 15 mm, respectively, resulting in an average initial stiffness of $K_{net,ini} = 0.03585$ N/mm. The initial stiffness of the device, $K_{pnsd,ini}$, for PNSD-1 was determined by subtracting $K_{MF} = 0.0407$ N/mm from $K_{net,ini}$ to be $K_{pnsd,ini} = K_{net,ini} - K_{MF} = -0.00485$ N/mm, exhibiting a negative stiffness. Similarly, the second stiffness of the vibrating system $K_{net,sec}$ was calculated using the inertial force–displacement data under an amplitude input of 15 mm, as shown in Fig. 9(d), where snap-through buckling was observed most prominently, as illustrated in Fig. 10(d). The least-square approximation method used the data within a positive displacement in the range of 45–51 mm, where $K_{net,sec}$ was approximately 0.0308 N/mm. The second stiffness of the device $K_{pnsd,sec}$ for PNSD-1 was computed as $K_{pnsd,sec} = K_{net,sec} - K_{MF} = -0.0099$ N/mm, which was approximately twice the initial negative stiffness $K_{pnsd,ini} = -0.00485$ N/mm.

In addition, Figs. 11 and 12 display the response loops for the vibrating system with PNSD-2 and the subtracted loops of PNSD-2 under sinusoidal waves (amplitudes: 12, 13, 15, and 18 mm, frequency: 1.0 Hz). Similarly, Figs. 13 and 14 show the response and subtracted loops of PNSD-3 subjected to sinusoidal waves (amplitudes: 10, 12, 13, and 15 mm, frequency: 1.0 Hz). For obtaining a wide range of response

displacement including before and after the onset of snap-through buckling, a different combination of input displacement amplitudes was used in PNSD-2 from those used in PNSD-1 and PNSD-3. The initial and second stiffnesses of PNSD-2 and PNSD-3 were assessed using the same methodology; Table 3 presents the results with the three PNSDs. In addition, the initial and second stiffness ratios calculated as $K_{pnsd,ini}/K_{MF}$ and $K_{pnsd,sec}/K_{MF}$, respectively, for each PNSD are listed in Table 3. The second negative stiffness for PNSD-2 was approximately twice the initial negative stiffness. Moreover, approximately double the initial and second negative stiffnesses were obtained for PNSD-2 compared to those for PNSD-1, which was attributed to the larger plate width of PNSD-2 compared with that of PNSD-1 (Table 1). However, although the initial stiffness for PNSD-3 exhibited a positive value, the second stiffness exhibited a negative value owing to the onset of snap-through buckling.

(c) Section force in hysteresis loops with PNSDs.

According to Figs. 10, 12, and 14, the maximum section force (intercept) of the subtracted force at the neutral displacement for the three PNSDs was roughly in the range of 0.15–0.31 N. A comparison between these section forces and that of SDOF-MF (approximately 0.24 N) reveals that installing the PNSDs did not significantly increase the section force. Thus, the energy consumption, such as the friction between the leaf springs of the PNSDs, was small. This indicates that the seismic response control effects achieved by the installation of the PNSDs in the shake table experiments were not due to energy absorption by the frictional force of the PNSDs, but due to the connection effects by negative stiffness.

(d) Time-history response with the PNSDs.

Fig. 15 shows the time-history displacement and acceleration of the mainframe for CVC-1 with PNSD-1 under sinusoidal wave input
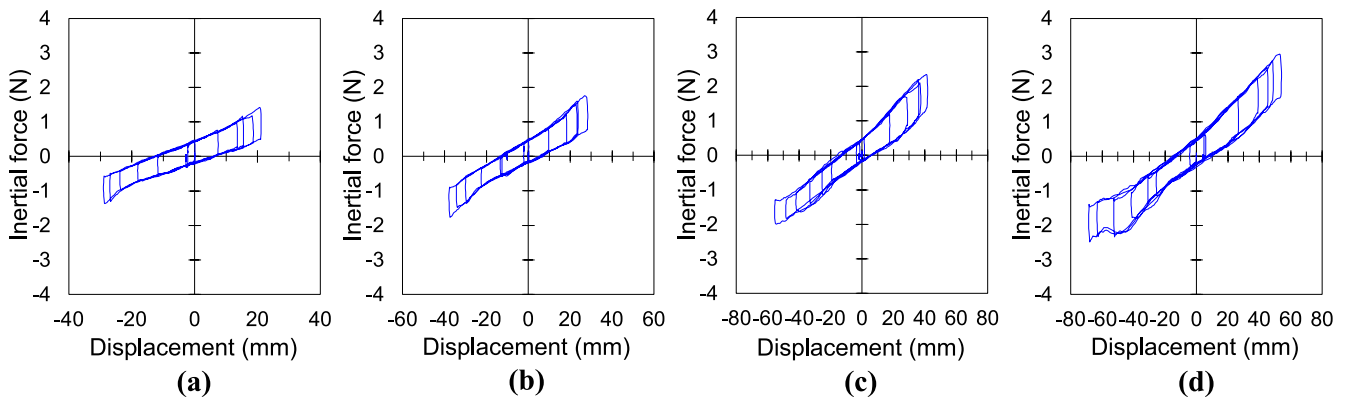

Fig. 11. Response hysteresis loops of the vibrating system (the mainframe with PNSD-2 and fixed-subframe) under the sinusoidal waves (frequency: 1.0 Hz) obtained from the experiments: **(a)** input amplitude: 12 mm; **(b)** input amplitude: 13 mm; **(c)** input amplitude: 15 mm; and **(d)** input amplitude: 18 mm.
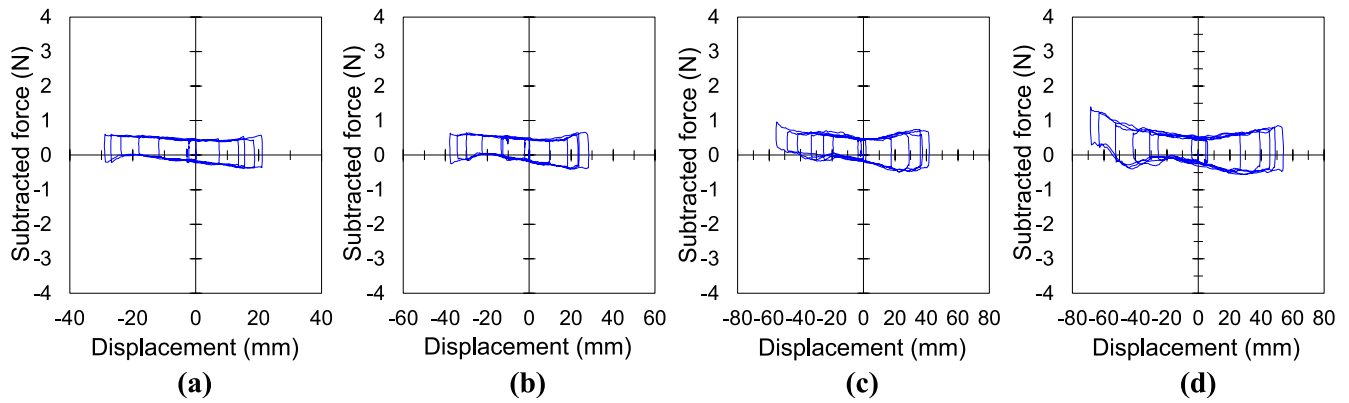
Fig. 12. Subtracted hysteresis loops for PNSD-2 under the sinusoidal wave (frequency: 1.0 Hz) obtained from the experiments: **(a)** input amplitude: 12 mm; **(b)** input amplitude: 13 mm; **(c)** input amplitude: 15 mm; and **(d)** input amplitude: 18 mm.
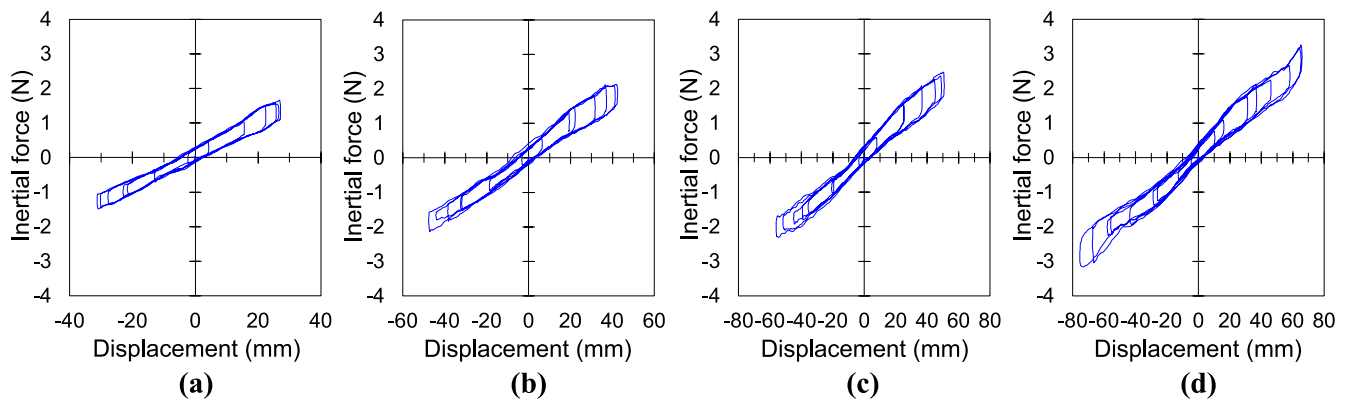

Fig. 13. Response hysteresis loops of the vibrating system (the mainframe with PNSD-3 and fixed-subframe) under the sinusoidal waves (frequency: 1.0 Hz) obtained from the experiments: **(a)** input amplitude: 10 mm; **(b)** input amplitude: 12 mm; **(c)** input amplitude: 13 mm; and **(d)** input amplitude: 15 mm.
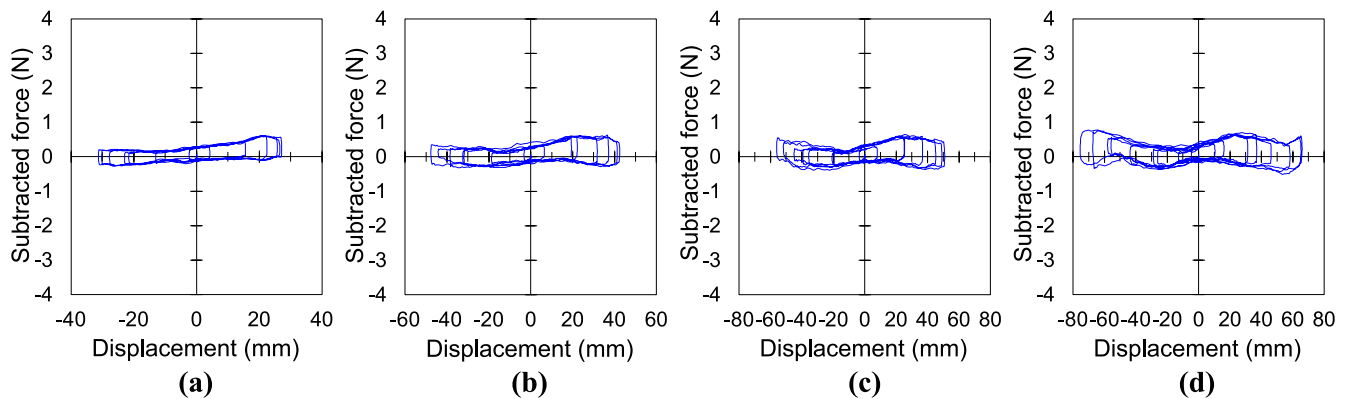

Fig. 14. Subtracted hysteresis loops for PNSD-3 under the sinusoidal wave (frequency: 1.0 Hz) obtained from the experiments: **(a)** input amplitude: 10 mm; **(b)** input amplitude: 12 mm; **(c)** input amplitude: 13 mm; and **(d)** input amplitude: 15 mm.

(frequency: 1.0 Hz, amplitude: 10 mm); in addition, it shows the waveform of the SDOF-MF without PNSD. Indeed, the vibrating period of the response displacement and acceleration waveforms for CVC-1 was lengthened compared with that without PNSD. This period lengthening was primarily attributed to the negative-stiffness effect of PNSD-1. Furthermore, a clear response reduction was observed in CVC-1 compared to the case without PNSD. This response reduction was owing to the effect of avoiding resonance by period lengthening and increased damping by the CVC effect. Moreover, the time-history waveforms for CVC-2 and CVC-3 under sinusoidal wave inputs are shown in Figs. 16 and 17, respectively. A similar tendency to CVC-1 is

observed for CVC-2, proving a significant response reduction and lengthening of the vibration period by incorporating PNSD-2. In contrast, a shortening of the vibration period for CVC-3 is observed after the installation of PNSD-3, which is due to the positive initial stiffness of PNSD-3 presented in Table 3.

2.3.3. Results under simulated wave inputs

Table 4 lists the peak displacement (PD) of the mainframe for each specimen (mean value of the five simulated waves) under each input magnification. In Table 4, $PD_{1,MF}$, $PD_{2,MF}$, $PD_{3,MF}$, $PD_{R,MF}$, and $PD_{SDOF,MF}$ represent the peak displacements of the mainframe for CVC-1, CVC-2,

Table 3

Evaluated stiffness of PNSDs obtained from the experiments.

Device name	PNSD-1	PNSD-2	PNSD-3
Displacement range for evaluation of the initial stiffness (mm)	−10 to + 10	−10 to + 10	−10 to + 10
Initial stiffness of the device (N/mm)	−0.00485	−0.009475	0.00755
Initial stiffness ratio	−0.12	−0.23	0.19
Displacement range for evaluation of the second stiffness (mm)	+45 to + 51	−48 to − 42	−42 to − 36
Second stiffness of the device (N/mm)	−0.0099	−0.0192	−0.0061
Second stiffness ratio	−0.24	−0.47	−0.15

CVC-3, CVC-R, and SDOF-MF, respectively. According to Table 4, the peak displacement of the mainframe for CVC-1, CVC-2, and CVC-3 is lower than that of SDOF-MF. Moreover, the peak displacement of CVC-2 is lower than that of CVC-R, exhibiting a better displacement control effect. Similarly, Table 5 presents the peak acceleration (PA) of the mainframe for each specimen (mean value of the five simulated waves) under each input magnification. Furthermore, $PA_{1,MF}$, $PA_{2,MF}$, $PA_{3,MF}$, $PA_{R,MF}$, and $PA_{SDOF,MF}$ represent the peak acceleration of the mainframe for CVC-1, CVC-2, CVC-3, CVC-R, and SDOF-MF, respectively. According

to Table 5, the peak accelerations for CVC-1 and CVC-2 are lower than that of SDOF-MF. Moreover, the peak acceleration of CVC-1, CVC-2, and CVC-3 are lower than that of CVC-R, exhibiting a high acceleration control reduction effect. However, the peak acceleration of the mainframe for CVC-3 was close to that of CVC-R.

The reduction indices of the peak displacement and acceleration of the mainframe for CVC-1 compared with those of SDOF-MF were calculated as $RD_{1,MF} = 1 − (PD_{1,MF}/PD_{SDOF,MF})$ and $RA_{1,MF} = 1 − (PA_{1,MF}/PA_{SDOF,MF})$, respectively. Similarly, the reduction index for CVC-2
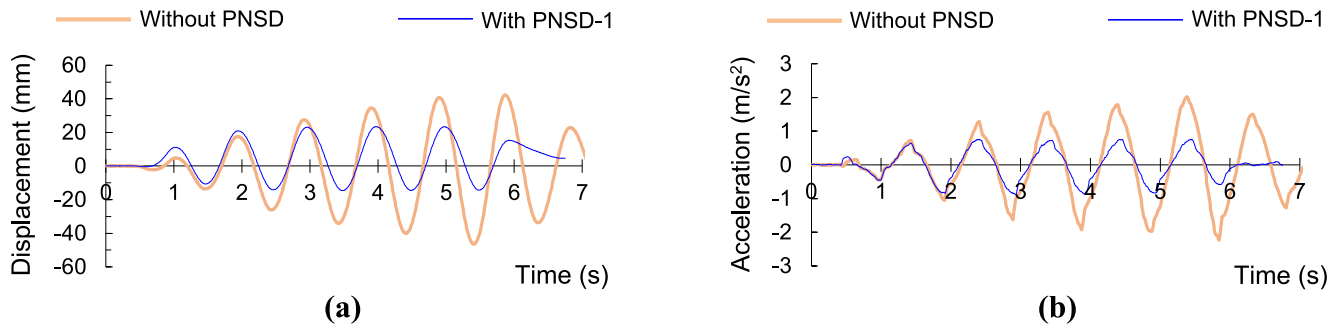

Fig. 15. Time-history response of the mainframe for CVC-1 with PNSD-1 and SDOF-MF without PNSD under the sinusoidal wave input (frequency: 1.0 Hz, input amplitude: 10 mm) obtained from the experiments: **(a)** displacement; and **(b)** acceleration.

Fig. 16. Time-history response of the mainframe for CVC-2 with PNSD-2 and SDOF-MF without PNSD under the sinusoidal wave input (frequency: 1.0 Hz, input amplitude: 10 mm) obtained from the experiments: **(a)** displacement; and **(b)** acceleration.
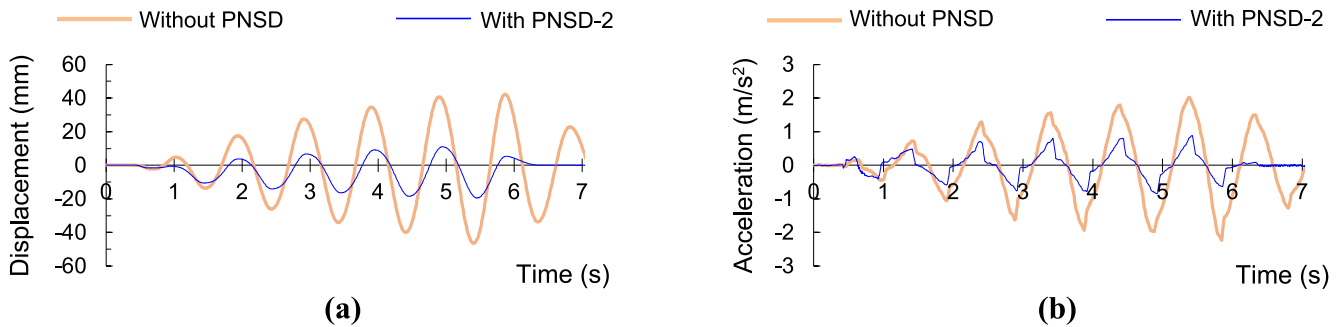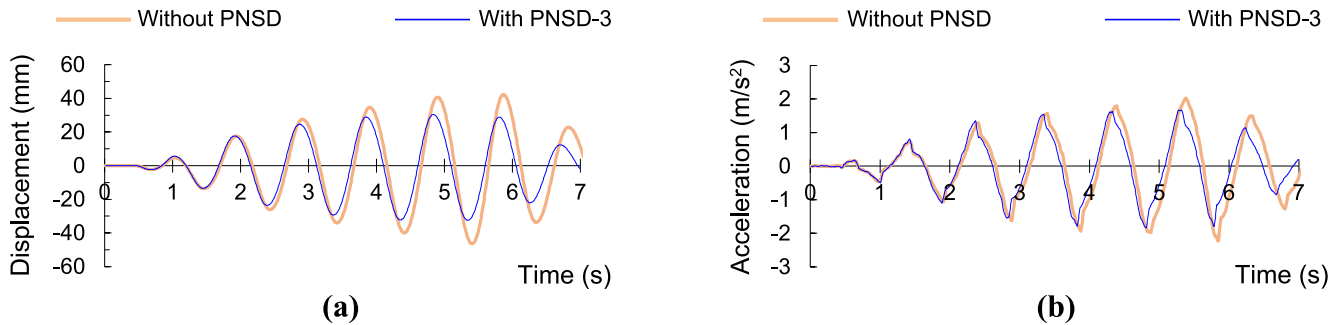

Fig. 17. Time-history response of the mainframe for CVC-3 with PNSD-3 and SDOF-MF without PNSD under the sinusoidal wave input (frequency: 1.0 Hz, input amplitude: 10 mm) obtained from the experiments: **(a)** displacement; and **(b)** acceleration.

Table 4

Peak displacements of the mainframe for CVC-R, SDOF-MF, CVC-1, CVC-2, and CVC-3 obtained from the experiments [mean value of the five simulated waves (Waves S1–5)].

Input magnification	Peak displacement for CVC-R ($PD_{R,MF}$) (mm)	Peak displacement for SDOF-MF ($PD_{SDOF,MF}$) (mm)	Peak displacement for CVC-1 ($PD_{1,MF}$) (mm)	Peak displacement for CVC-2 ($PD_{2,MF}$) (mm)	Peak displacement for CVC-3 ($PD_{3,MF}$) (mm)
0.20	10.61	12.47	12.17	8.85	10.72
0.30	20.33	24.65	20.61	16.27	21.55
0.40	30.35	37.32	29.57	25.02	34.52
0.45	35.65	43.56	34.31	29.41	40.59
0.50	40.17	50.60	40.47	33.55	47.78

Table 5

Peak accelerations of the mainframe for CVC-R, SDOF-MF, CVC-1, CVC-2, and CVC-3 obtained from the experiments [mean value of the five simulated waves (Waves S1–5)].

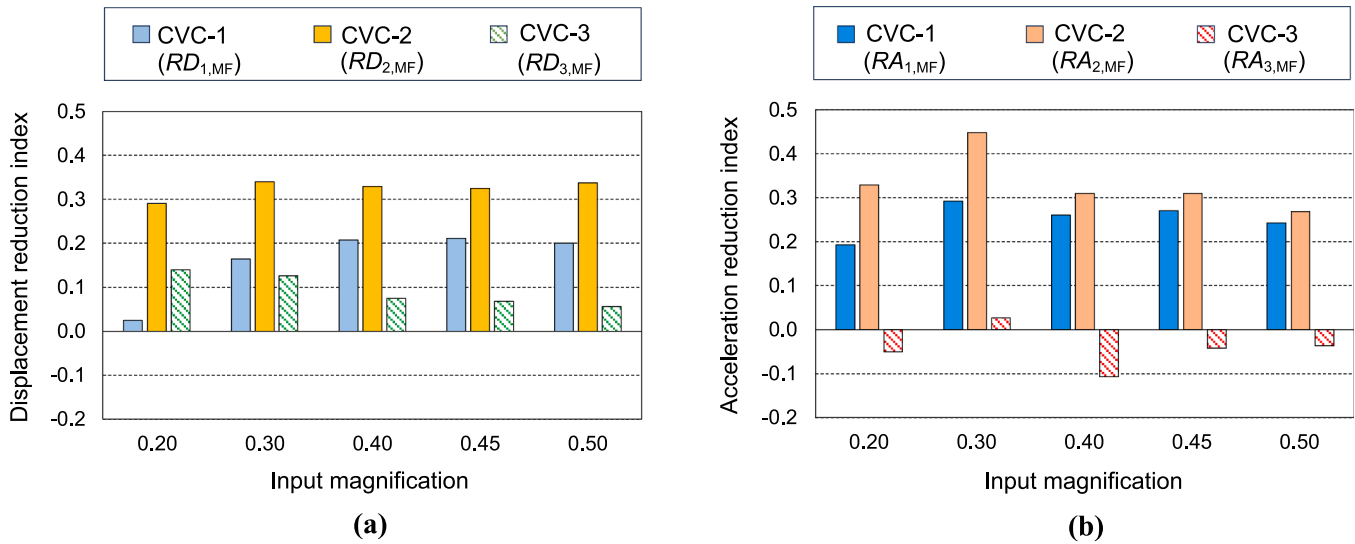| Input magnification	Peak acceleration for CVC-R ($PA_{R,MF}$) (m/s²)	Peak acceleration for SDOF-MF ($PA_{SDOF,MF}$) (m/s²)	Peak acceleration for CVC-1 ($PA_{1,MF}$) (m/s²)	Peak acceleration for CVC-2 ($PA_{2,MF}$) (m/s²)	Peak acceleration for CVC-3 ($PA_{3,MF}$) (m/s²)
0.20	0.747	0.669	0.540	0.449	0.702
0.30	1.358	1.336	0.946	0.738	1.299
0.40	1.983	1.776	1.312	1.226	1.966
0.45	2.324	2.115	1.544	1.460	2.204
0.50	2.607	2.417	1.829	1.766	2.506

Fig. 18. Reduction indices of the peak response of the mainframe for CVC-1, CVC-2, and CVC-3 compared with SDOF-MF under the simulated waves for each input magnification (mean value of the five simulated waves) obtained from the experiments: **(a)** displacement reduction index; and **(b)** acceleration reduction index.

was calculated as $RD_{2,MF} = 1 - (PD_{2,MF}/PD_{SDOF,MF})$ and $RA_{2,MF} = 1 - (PA_{2,MF}/PA_{SDOF,MF})$, whereas the reduction index for CVC-3 was calculated as $RD_{3,MF} = 1 - (PD_{3,MF}/PD_{SDOF,MF})$ and $RA_{3,MF} = 1 - (PA_{3,MF}/PA_{SDOF,MF})$. Fig. 18(a) and (b) show the calculated reduction indices for the displacement and acceleration, respectively (mean value of the five simulated waves). The reduction indices for displacement show promising results, particularly for CVC-1 and CVC-2. A comparison of the reduction indices in Fig. 18(a) reveals that PNSD-2 performs better than PNSD-1 and PNSD-3. Moreover, reasonable acceleration reduction indices for the mainframe were obtained for CVC-1 and CVC-2, especially PNSD-2 achieved a better acceleration reduction, as presented in Fig. 18(b).

Fig. 19 shows the response time-history displacement and acceleration of CVC-1 with PNSD-1 subjected to Wave S5 (input magnification: 0.45). In addition, the responses of SDOF-MF without PNSD are compared. Fig. 19 shows that incorporating PNSD-1 reduces both the displacement and acceleration responses of the mainframe compared with SDOF-MF without PNSD over the main duration of the seismic excitation. Similarly, Figs. 20 and 21 depict the time-history response for

the mainframe of CVC-2 with PNSD-2 and CVC-3 with PNSD-3, respectively, subjected to Wave S5 (input magnification: 0.45). A similar or better response reduction compared to CVC-1 (Fig. 19) was observed for CVC-2 (Fig. 20), whereas sufficient response reduction was not achieved for the mainframe of CVC-3, as shown in Fig. 21.

Fig. 22 illustrates the reduction ratios of the peak response displacement and acceleration for the mainframe and subframe of CVC-1 under the simulated waves for each input magnification. The displacement reduction ratio is the ratio of the peak displacement for the mainframe (or subframe) of CVC-1 (mean value of the five simulated waves) to that of SDOF-MF (or SDOF-SF). Similarly, the acceleration reduction ratio is the ratio of the averaged peak acceleration of the mainframe (or subframe) of CVC-1 to that of SDOF-MF (or SDOF-SF). According to Fig. 22, the results exhibit a clear reduction in the displacement and acceleration responses for the mainframe of CVC-1 compared to SDOF-MF for all input magnification. However, the displacement and acceleration reduction ratios of the subframe in CVC-1 exceed unity, indicating an increase in the response of the subframe compared to SDOF-SF. In addition, Figs. 23 and 24 show response
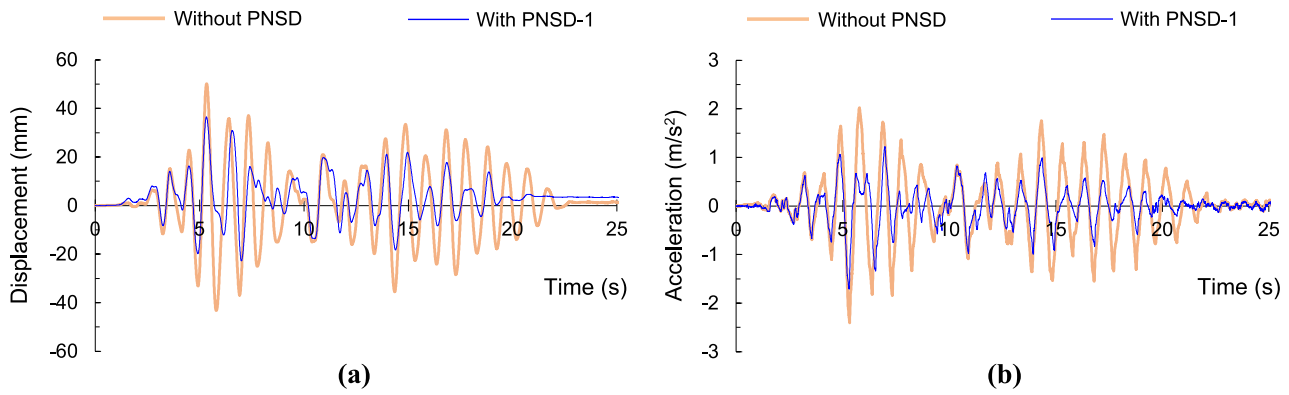
Fig. 19. Time-history response of the mainframe for CVC-1 with PNSD-1 and SDOF-MF without PNSD subjected to Wave S5 (input magnification: 0.45) obtained from the experiments: **(a)** displacement; and **(b)** acceleration.

reduction ratios for CVC-2 and CVC-3, respectively. According to Fig. 24, although CVC-3 decreases the displacement reduction ratio to lower than unity for both the mainframe and subframe, the acceleration reduction ratio of the mainframe becomes larger than unity. This larger acceleration ratio in CVC-3 may be due to the positive initial stiffness before snap-through buckling of PNSD-3, as presented in Table 3, which challenges achieving a proper control tuning. According to Fig. 23, a significant decrease in displacement and acceleration is achieved for the mainframe of CVC-2. Moreover, for the subframe of CVC-2, the displacement and acceleration are clearly reduced except the displacement under the input magnification of 0.2. Therefore, CVC-2 yielded the most promising response control effects among the three PNSDs. Consequently, an effective response control for the mainframe against seismic excitations was achieved by incorporating PNSDs as the connector of the CVC system.

3. Numerical simulations

A time-history simulation was performed to explore the response behavior and assess the control effects of multistory CVC buildings incorporating negative stiffness at the connection when subjected to seismic ground motions.

3.1. Simulation methods

3.1.1. Numerical building models

The simulation used the CVC-NV, CVC-V, UC-MF, and UC-SF models as numerical six-story building models. Fig. 25 shows the four numerical models. The CVC-NV model is a CVC system comprising a 6DOF mainframe structure, 6DOF subframe structure, and negative-stiffness spring

and dashpot element as the connectors, as shown in Fig. 25(a). The CVC-V model is another CVC system comprising a mainframe, subframe, and dashpot element connector, as shown in Fig. 25(b). For the CVC models, the connecting elements were placed between the sixth floor of the mainframe and subframe, as illustrated in Fig. 25(a) and (b). The UC-MF and UC-SF models were uncontrolled systems, which were the mainframe alone, as shown in Fig. 25(c), and subframe alone, as shown in Fig. 25(d). As inherent damping, a viscous damping element was placed for each story of the mainframe and subframe such that a stiffness-proportional damping (damping ratio of 2% for the first vibrational mode) was obtained for each of the UC-MF and UC-SF models. The parameters of the mainframe and subframe were identical among the four models.

Two parameter combinations, namely Cases I and II, were examined based on the mass ratio μ' and stiffness ratio α'. The mass ratio μ' is defined as $\mu' = m_i^S/m_i^M$, where m_i^S and m_i^M denote the mass of the subframe and mainframe for the ith story, respectively. The stiffness ratio α' is defined as $\alpha' = k_i^S/k_i^M$, where k_i^S and k_i^M denote the stiffness of the subframe and mainframe for the ith story, respectively. In Case I, a combination of $\alpha' = 1.0$ and $\mu' = 0.5$, was adopted, whereas in Case II, a combination of $\alpha' = 0.2$ and $\mu' = 0.1$ was used. Tables 6 and 7 list the structural properties of the mainframe and subframe for Cases I and II, respectively. A mass of 1000 t was set for each story of the mainframe for both Cases I and II. The mainframe stiffness for each story was linearly distributed in a proportion ratio in the range of 1.0–2.0, from the top to bottom stories, such that the first modal natural period of the UC-MF model was $T = 0.72$ s. Thus, the first modal natural period of UC-SF was 0.51 s for both Cases I and II. In addition, the combination of the stiffness and mass ratios used in Case I ($\alpha' = 1.0$ and $\mu' = 0.5$) was similar to that in the shake table experiments discussed in Section 2 ($\alpha = 1.0$, $\mu =$
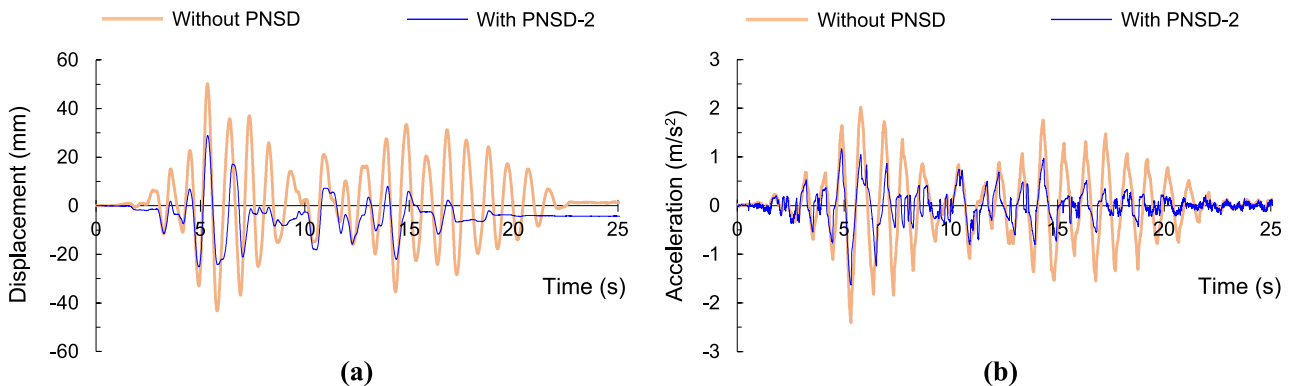

Fig. 20. Time-history response of the mainframe for CVC-2 with PNSD-2 and SDOF-MF without PNSD subjected to Wave S5 (input magnification: 0.45) obtained from the experiments: **(a)** displacement; and **(b)** acceleration.
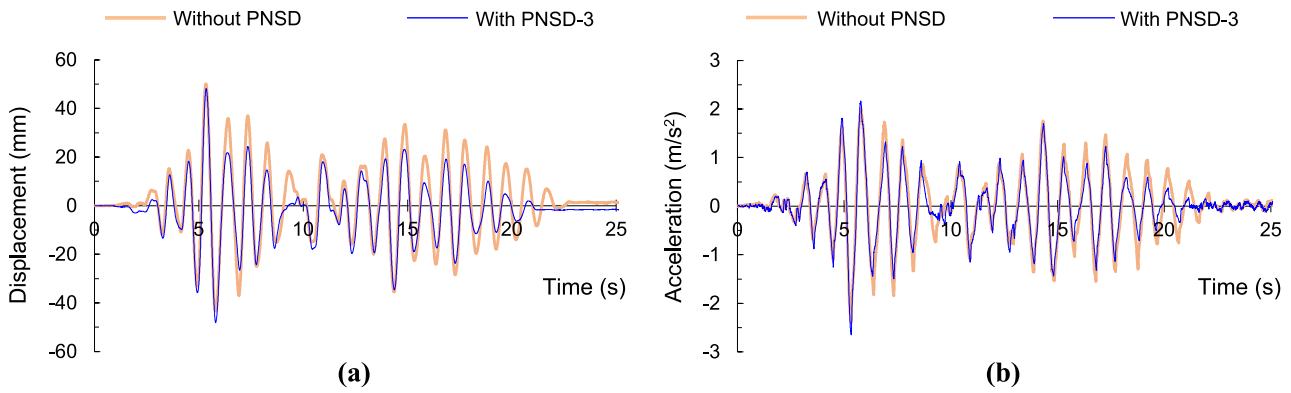
Fig. 21. Time-history response of the mainframe for CVC-3 with PNSD-3 and SDOF-MF without PNSD subjected to Wave S5 (input magnification: 0.45) obtained from the experiments: **(a)** displacement; and **(b)** acceleration.

Fig. 22. Reduction ratio of the peak response of the mainframe (or subframe) for CVC-1 to that of SDOF-MF (or SDOF-SF) under the simulated waves (averaged for the five simulated waves) obtained from the experiments: **(a)** displacement reduction ratio; and **(b)** acceleration reduction ratio.
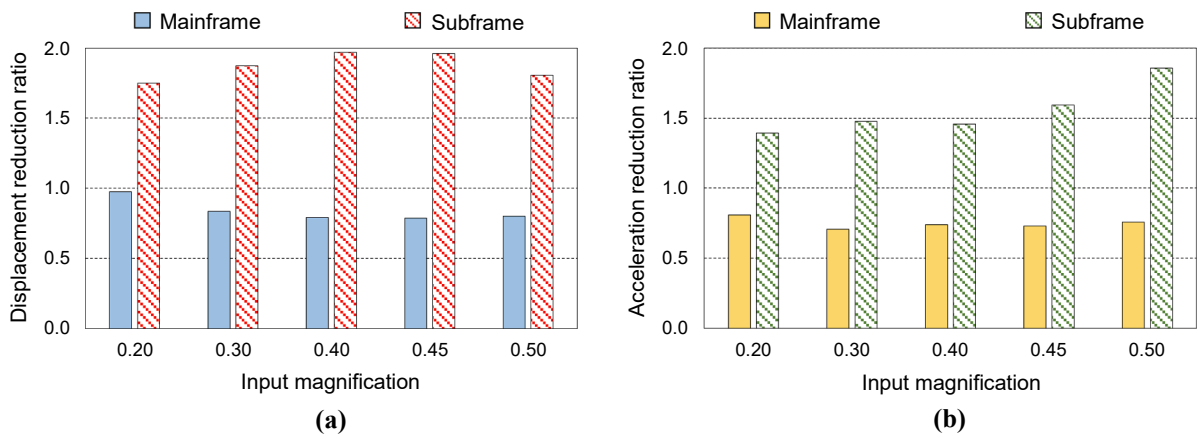

Fig. 23. Reduction ratio of the peak response of the mainframe (or subframe) for CVC-2 to that of SDOF-MF (or SDOF-SF) under the simulated waves (averaged for the five simulated waves) obtained from the experiments: **(a)** displacement reduction ratio; and **(b)** acceleration reduction ratio.

0.5). In addition, for making it easier to associate the structural parameter conditions and obtained results of the numerical CVC building models (such as α' and μ') with those of the one-story CVC specimens of the shake table experiments (such as α and μ), the mainframe and subframe of the six-story models in the numerical simulation were connected at the sixth floors, which are closer to the equivalent height when the six-story mainframe and subframe are converted into the equivalent one-story systems.

Table 8 lists the parameters of the negative-stiffness spring and dashpot elements at the connection of the CVC models in Cases I and II. In addition, the simulation targeted the control of the mainframe response and did not apply an optimization method to the parameter setting.

3.1.2. Equation of motions
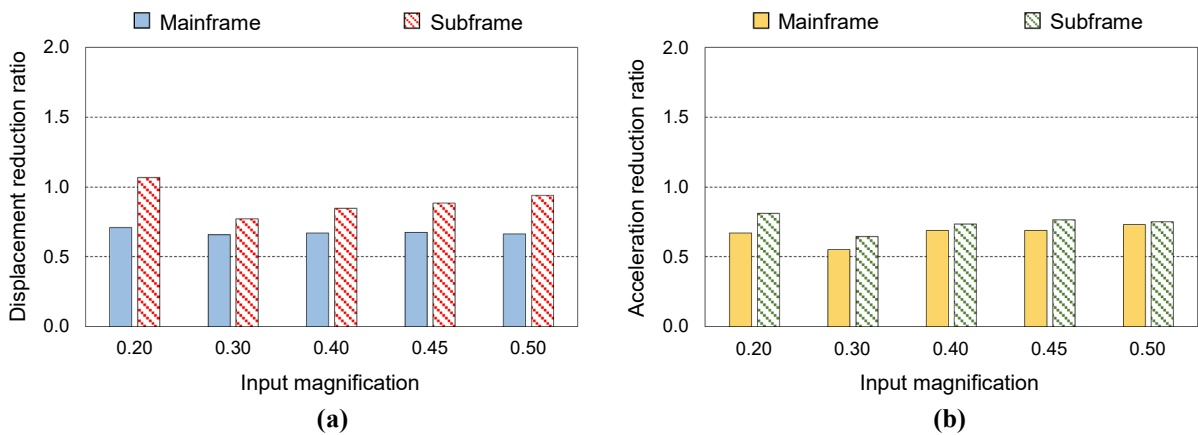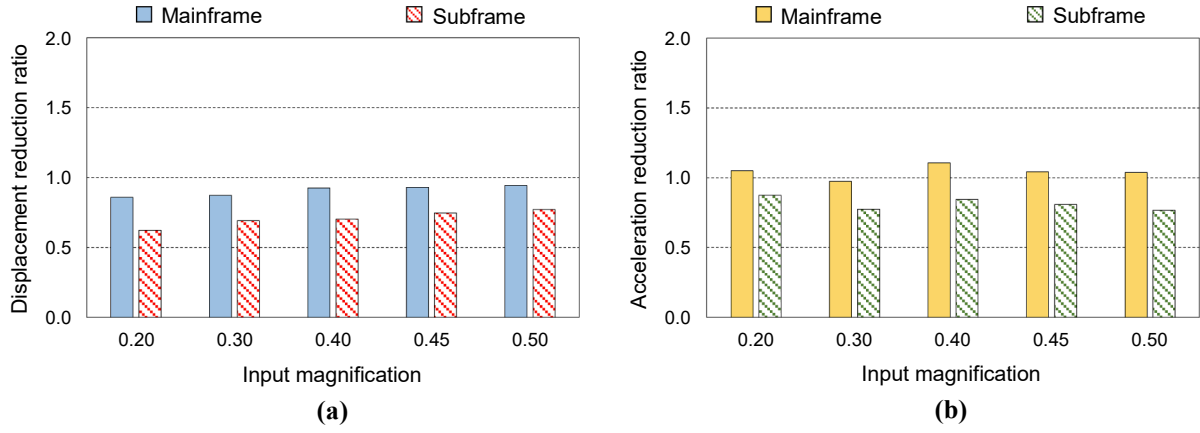The governing equation of motion for the six-story CVC system

Fig. 24. Reduction ratio of the peak response of the mainframe (or subframe) for CVC-3 to that of SDOF-MF (or SDOF-SF) under the simulated waves (averaged for the five simulated waves) obtained from the experiments: **(a)** displacement reduction ratio; and **(b)** acceleration reduction ratio.
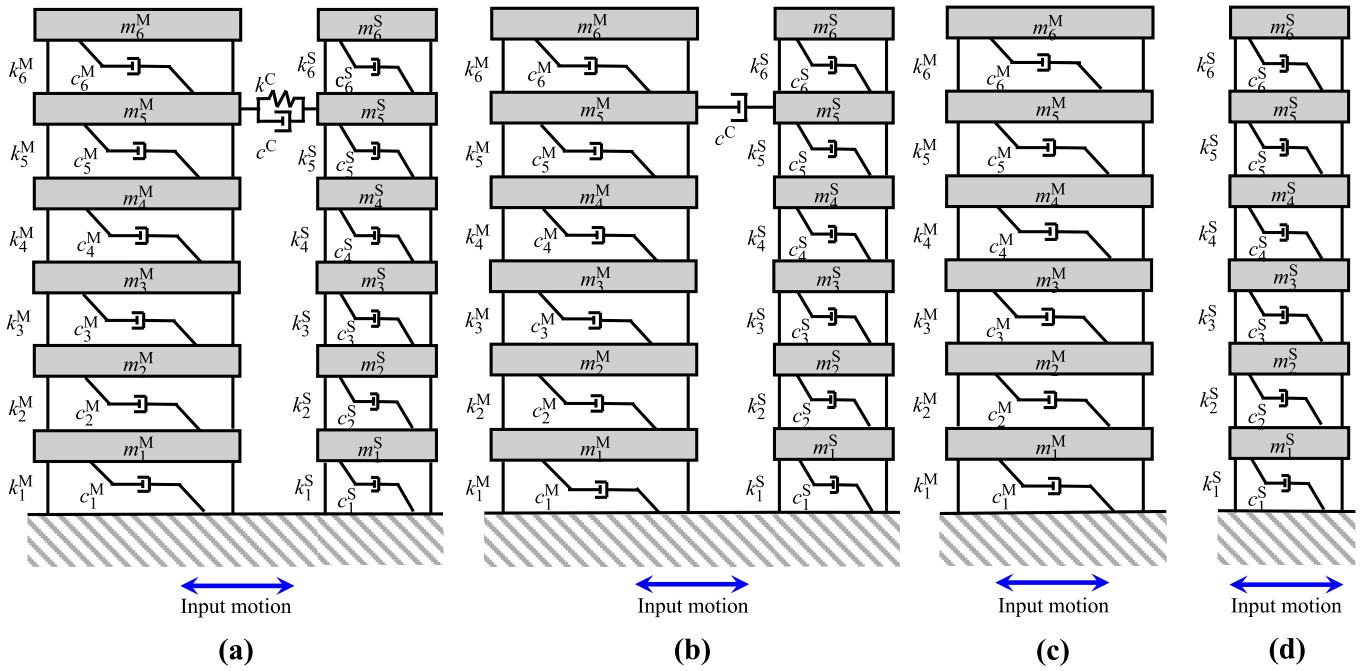

Fig. 25. Numerical building models: **(a)** CVC-NV model with a dashpot and negative stiffness spring connectors; **(b)** CVC-V model with a dashpot connector; **(c)** UC-MF model; and **(d)** UC-SF model.

Table 6
Properties of the 6DOF mainframe and subframe numerical models for Case I.

Story, i	Mainframe			Subframe		
	Mass, m_i^M (t)	Stiffness,k_i^M (MN/m)	Damping coefficient,c_i^M (MNs/m)	Mass, m_i^S (t)	Stiffness,k_i^S (MN/m)	Damping coefficient,c_i^S (MNs/m)
6	1000	790.9	3.625	500	790.9	2.563
5	1000	949.1	4.350	500	949.1	3.076
4	1000	1107.2	5.075	500	1107.2	3.589
3	1000	1265.4	5.800	500	1265.4	4.101
2	1000	1423.6	6.525	500	1423.6	4.614
1	1000	1581.8	7.250	500	1581.8	5.127

consisting of a 6DOF mainframe and subframe can be expressed as [6,9]:

$$\mathbf{M}\ddot{\mathbf{x}}(t) + \mathbf{C}\dot{\mathbf{x}}(t) + \mathbf{K}\mathbf{x}(t) = -\mathbf{M}\ \mathbf{1}\ \ddot{x}_G(t) \tag{2}$$

where $\mathbf{M}$ is the mass matrix, $\mathbf{C}$ is the damping matrix, $\mathbf{K}$ is the stiffness matrix, t is the time, $\ddot{\mathbf{x}}(t)$ is the relative response acceleration vector, $\dot{\mathbf{x}}(t)$ is the response velocity vector, $\mathbf{x}(t)$ is the response displacement vector,

$\ddot{x}_G(t)$ is the input acceleration, and $\mathbf{1}$ is a column vector of dimension 12, with all entries equal to 1. Moreover, $\ddot{\mathbf{x}}(t)$, $\dot{\mathbf{x}}(t)$, and $\mathbf{x}(t)$ can be expressed as follows:

$$\ddot{\mathbf{x}}(t) = \left[\ddot{x}_1^M(t)\ddot{x}_2^M(t)\cdots\ddot{x}_6^M(t)\ddot{x}_1^S(t)\ddot{x}_2^S(t)\cdots\ddot{x}_6^S(t) \right]^T \tag{3}$$

Table 7
Properties of the 6DOF mainframe and subframe numerical models for Case II.

Story, i	Mainframe			Subframe		
	Mass, m_i^M (t)	Stiffness, k_i^M (MN/m)	Damping coefficient, c_i^M (MNs/m)	Mass, m_i^S (t)	Stiffness, k_i^S (MN/m)	Damping coefficient, c_i^S (MNs/m)
6	1000	790.9	3.625	100	158.2	0.513
5	1000	949.1	4.350	100	189.8	0.615
4	1000	1107.2	5.075	100	221.4	0.718
3	1000	1265.4	5.800	100	253.1	0.820
2	1000	1423.6	6.525	100	284.7	0.923
1	1000	1581.8	7.250	100	316.4	1.025

$$\dot{\mathbf{x}}(t) = \begin{bmatrix} \dot{x}_1^M(t) & \dot{x}_2^M(t) & \cdots & \dot{x}_6^M(t) & \dot{x}_1^S(t) & \dot{x}_2^S(t) & \cdots & \dot{x}_6^S(t) \end{bmatrix}^T \tag{4}$$

$$\mathbf{x}(t) = \begin{bmatrix} x_1^M(t) & x_2^M(t) & \cdots & x_6^M(t) & x_1^S(t) & x_2^S(t) & \cdots & x_6^S(t) \end{bmatrix}^T \tag{5}$$

where $\ddot{x}_i^M(t)$ and $\ddot{x}_i^S(t)$ represent the relative acceleration responses, $\dot{x}_i^M(t)$ and $\dot{x}_i^S(t)$ represent the velocity responses, and $x_i^M(t)$ and $x_i^S(t)$ represent the displacement responses at the ith story for the mainframe and subframe, respectively.

The mass matrix $\mathbf{M}$ for all four models (CVC-NV, CVC-V, UC-MF, and UC-SF) can be expressed as follows:

$$\mathbf{M} = \begin{bmatrix} \mathbf{M^M} & \mathbf{0} \\ \mathbf{0} & \mathbf{M^S} \end{bmatrix} \tag{6}$$

$$\mathbf{M^M} = \begin{bmatrix} m_1^M & \cdots & 0 \\ \vdots & \ddots & \vdots \\ 0 & \cdots & m_6^M \end{bmatrix} \tag{7}$$

$$\mathbf{M^S} = \begin{bmatrix} m_1^S & \cdots & 0 \\ \vdots & \ddots & \vdots \\ 0 & \cdots & m_6^S \end{bmatrix} \tag{8}$$

where $\mathbf{M^M}$ is the mass matrix for the mainframe, $\mathbf{M^S}$ is the mass matrix for the subframe, m_i^M is the mass of the ith story of the mainframe, m_i^S is the mass of the ith story of the subframe, and $\mathbf{0}$ is a zero matrix of dimensions 6×6.

The stiffness matrix $\mathbf{K}$ for the uncontrolled models (UC-MF and UC-SF) can be expressed as follows:

$$\mathbf{K} = \begin{bmatrix} \mathbf{K^M} & \mathbf{0} \\ \mathbf{0} & \mathbf{K^S} \end{bmatrix} \tag{9}$$

$$\mathbf{K^M} = \begin{bmatrix} k_1^M + k_2^M & -k_2^M & \cdots & 0 \\ -k_2^M & \ddots & \ddots & \vdots \\ \vdots & \ddots & \ddots & -k_6^M \\ 0 & \cdots & -k_6^M & k_6^M \end{bmatrix} \tag{10}$$

$$\mathbf{K^S} = \begin{bmatrix} k_1^S + k_2^S & -k_2^S & \cdots & 0 \\ -k_2^S & \ddots & \ddots & \vdots \\ \vdots & \ddots & \ddots & -k_6^S \\ 0 & \cdots & -k_6^S & k_6^S \end{bmatrix} \tag{11}$$

where $\mathbf{K^M}$ is the stiffness matrix for the mainframe, $\mathbf{K^S}$ is the stiffness matrix for the subframe, k_i^M is the stiffness of the ith story of the mainframe, and k_i^S is the stiffness of the ith story of the subframe.

In addition, the damping matrix $\mathbf{C}$ for the uncontrolled models (UC-MF and UC-SF) can be expressed as follows:

$$\mathbf{C} = \begin{bmatrix} \mathbf{C^M} & \mathbf{0} \\ \mathbf{0} & \mathbf{C^S} \end{bmatrix} \tag{12}$$

$$\mathbf{C^M} = \begin{bmatrix} c_1^M + c_2^M & -c_2^M & \cdots & 0 \\ -c_2^M & \ddots & \ddots & \vdots \\ \vdots & \ddots & \ddots & -c_6^M \\ 0 & \cdots & -c_6^M & c_6^M \end{bmatrix} \tag{13}$$

$$\mathbf{C^S} = \begin{bmatrix} c_1^S + c_2^S & -c_2^S & \cdots & 0 \\ -c_2^S & \ddots & \ddots & \vdots \\ \vdots & \ddots & \ddots & -c_6^S \\ 0 & \cdots & -c_6^S & c_6^S \end{bmatrix} \tag{14}$$

where $\mathbf{C^M}$ is the damping matrix for the mainframe, $\mathbf{C^S}$ is the damping matrix for the subframe, c_i^M is the viscous damping coefficient for the ith story of the mainframe, and c_i^S is the viscous damping coefficient for the ith story of the subframe.

Moreover, the stiffness and damping matrices ($\mathbf{K}$ and $\mathbf{C}$) for the CVC-NV and CVC-V models can be expressed as follows:

$$\mathbf{K} = \begin{bmatrix} k_1^M + k_2^M & -k_2^M & \cdots & \cdots & \cdots & \cdots & \cdots & 0 \\ -k_2^M & \ddots & \ddots & \ddots & \ddots & \ddots & \ddots & \vdots \\ \vdots & \ddots & k_5^M + k_6^M + k^C & -k_6^M & \ddots & \ddots & -k^C & \vdots \\ \vdots & \ddots & -k_6^M & k_6^M & \ddots & \ddots & \ddots & \vdots \\ \vdots & \ddots & \ddots & \ddots & k_1^S + k_2^S & -k_2^S & \ddots & \vdots \\ \vdots & \ddots & \ddots & \ddots & -k_2^S & \ddots & \ddots & \vdots \\ \vdots & \ddots & -k^C & \ddots & \ddots & \ddots & k_5^S + k_6^S + k^C & -k_6^S \\ 0 & \cdots & \cdots & \cdots & \cdots & \cdots & -k_6^S & k_6^S \end{bmatrix} \tag{15}$$

$$\mathbf{C} = \begin{bmatrix} c_1^M + c_2^M & -c_2^M & \cdots & \cdots & \cdots & \cdots & \cdots & 0 \\ -c_2^M & \ddots & \ddots & \ddots & \ddots & \ddots & \ddots & \vdots \\ \vdots & \ddots & c_5^M + c_6^M + c^C & -c_6^M & \ddots & \ddots & -c^C & \vdots \\ \vdots & \ddots & -c_6^M & c_6^M & \ddots & \ddots & \ddots & \vdots \\ \vdots & \ddots & \ddots & \ddots & c_1^S + c_2^S & -c_2^S & \ddots & \vdots \\ \vdots & \ddots & \ddots & \ddots & -c_2^S & \ddots & \ddots & \vdots \\ \vdots & \ddots & -c^C & \ddots & \ddots & \ddots & c_5^S + c_6^S + c^C & -c_6^S \\ 0 & \cdots & \cdots & \cdots & \cdots & \cdots & -c_6^S & c_6^S \end{bmatrix} \tag{16}$$

where k^C is the stiffness of the negative-stiffness connector and c^C is the damping coefficient of the dashpot connector.

In Equation (15), when $k^C < 0$, negative stiffness is provided at the

Table 8
Stiffness of negative stiffness spring (k^C) and damping coefficient of dashpot element (c^C) at the connecting portion in CVC models.

| Model name | Case I | | Case II | |
	Stiffness, k^C (MN/m)	Damping coefficient, c^C (MNs/m)	Stiffness, k^C (MN/m)	Damping coefficient, c^C (MNs/m)
CVC-V	0	14.725	0	1.816
CVC-NV	−15.27	2.364	−9.797	0.467

connection. In Equation (16), when $c^C > 0$, a dashpot is provided at the connection. Equations (2)–(14) were used for the uncontrolled models (UC–MF and UC–SF). Moreover, for the CVC-NV and CVC-V models, Equations (2)–(5) were used as the equation of motion, while the mass, stiffness, and damping matrices expressed by Equations (6)–(8), (15), and (16), were adopted. For the CVC-NV model incorporating both negative-stiffness spring and dashpot element connectors, $k^C < 0$ in Equation (15) and $c^C > 0$ in Equation (16) were set, as presented in Table 8. For the CVC-V model incorporating only dashpot element connectors, $k^C = 0$ in Equation (15) and $c^C > 0$ in Equation (16) were set, as presented in Table 8.

3.1.3. Input motions and analysis conditions

The numerical earthquake response simulation used three simulated waves and six observed records for the ground motions. The three simulated waves consisted of waves M1–3 adopted from the literature [30]. These simulated waves were prepared by fitting to the target response spectrum of the Japanese building seismic code. The present numerical simulation adopted the simulated waves as an example of input motions with a constant spectral velocity response region. The six observed records consisted of HKD 127 (K-NET Oiwake), HKD 128 (K-NET Hayakita), and HKD 180 (K-NET Sapporo) for each North–South (NS) and East–West (EW) component observed in the 2018 Hokkaido Eastern Iburi Earthquake [31,32,33]. Regarding the observed records, as an example of seismic observation waveforms with various spectral characteristics, the six input waveforms were adopted in the present numerical simulation. Table 9 and Fig. 26 show the peak ground acceleration and response velocity spectra for the input motions.

In the time-history response simulation, the Newmark β method ($\beta = 1/4$) with a sampling frequency of 1.0 kHz was used in the numerical integration. The software MATLAB [34] was used in the numerical simulation. In addition, for comparative verification purposes, preliminary eigenvalue and seismic response analyses for the UC-MF, UC-SF, and CVC-V models were conducted using other structural analysis software as well as the present numerical simulation. Through a comparison of the results, the validity of the present numerical simulation was confirmed.

3.1.4. Evaluation criteria description

In reference to the literature [35], the performance of the control effects for the CVC-NV and CVC-V models was assessed based on the evaluation criteria, J_1 and J_2, defined in Equations (17) and (18).

$$J_1 = \frac{max|x_i(t)|_{CVC}}{max|x_i(t)|_{UC}} \tag{17}$$

$$J_2 = \frac{max|\ddot{x}_i(t) + \ddot{x}_G(t)|_{CVC}}{max|\ddot{x}_i(t) + \ddot{x}_G(t)|_{UC}} \tag{18}$$

where $x_i(t)$ is the relative response displacement to the ground at the ith story of the mainframe (or subframe), $\ddot{x}_i(t)$ is the response acceleration at the ith story of the mainframe (or subframe), the subscript UC denotes the uncontrolled models (UC-MF or UC-SF), and the subscript CVC denotes the CVC models (CVC-NV and CVC-V).

3.2. Simulation results

3.2.1. Peak response for each story

Figs. 27 and 28 illustrate the simulated peak story drift of the mainframe for each story of Cases I and II, respectively. Here, the peak response is the mean value for each input group (Waves M1–3, K-NET Oiwake EW and NS, K-NET Hayakita EW and NS, and K-NET Sapporo EW and NS). According to Figs. 27 and 28, the peak story drifts of the mainframe for the control models (CVC-NV and CVC-V) are significantly reduced compared with those of the uncontrolled model (UC-MF) for all input groups for both Cases I and II. In addition, Figs. 29 and 30 show the peak acceleration of the mainframe for Cases I and II, respectively (averaged for each input group). As shown in Figs. 29 and 30, the peak acceleration of the mainframe for the CVC-NV model is generally lower than that for the CVC-V and UC-MF models.

3.2.2. Reduction indices

Tables 10 and 11 list the reduction indices of the peak displacement and acceleration of the CVC models for Cases I and II. Here, the reduction indices are the mean values for the three simulated wave inputs and six observed record inputs. Moreover, $RD_{CVC-NV,MF}$ and $RD_{CVC-V,MF}$ are the mainframe displacement reduction indices of the CVC-NV and CVC-V models, respectively. In addition, $RA_{CVC-NV,MF}$ and $RA_{CVC-V,MF}$ are the acceleration reduction indices of the mainframe for the CVC-NV and CVC-V models, respectively. $RD_{CVC-NV,MF}$ was calculated as $RD_{CVC-NV,MF} = 1 - (PD_{CVC-NV,MF}/PD_{UC-MF})$, where ($PD_{CVC-NV,MF}/PD_{UC-MF}$) is the ratio of the peak relative displacement to the ground for each story of the CVC-NV model to that of the UC-MF model, which is averaged for all six stories. In addition, $RD_{CVC-V,MF}$, $RA_{CVC-NV,MF}$, and $RA_{CVC-V,MF}$ were calculated similar to $RD_{CVC-NV,MF}$. According to Table 10, the displacement reduction index of the mainframe for the CVC-NV model ($RD_{CVC-NV,MF}$) yielded better results than that of the CVC-V model ($RD_{CVC-V,MF}$)
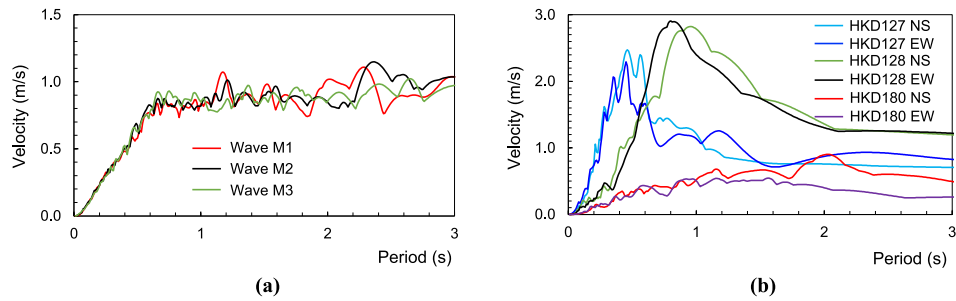
Table 9
Peak ground acceleration of the input motions for the numerical simulation.

Wave type	Input motion name	Peak ground acceleration (m/s^2)
Simulated wave	Wave M1	4.19
	Wave M2	3.80
	Wave M3	3.39
Observed record (2018 Hokkaido Eastern Iburi Earthquake)	HKD 127 (K-NET Oiwake) NS	10.04
	HKD 127 (K-NET Oiwake) EW	9.04
	HKD 128 (K-NET Hayakita) NS	5.56
	HKD 128 (K-NET Hayakita) EW	6.72
	HKD 180 (K-NET Sapporo) NS	1.43
	HKD 180 (K-NET Sapporo) EW	1.54

Fig. 26. Velocity response spectra of the input motions used in the numerical simulation (damping ratio: 0.05): **(a)** simulated waves; and **(b)** observed records.
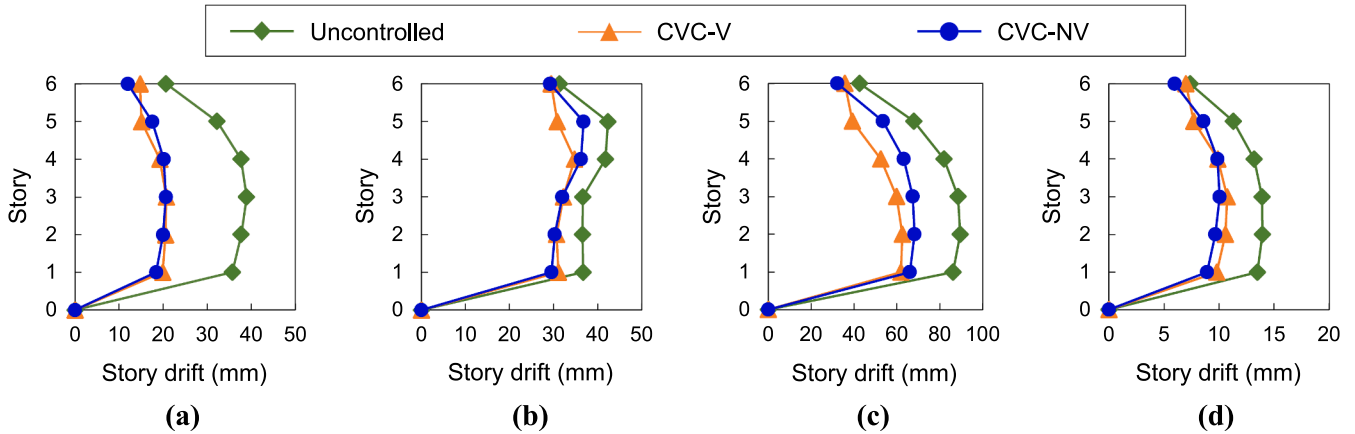

Fig. 27. Peak story drift of the mainframe for Case I obtained from the numerical simulation (averaged for each input group): **(a)** simulated waves (Waves M1–3); **(b)** K-NET Oiwake (EW and NS); **(c)** K-NET Hayakita (EW and NS); and **(d)** K-NET Sapporo (EW and NS).
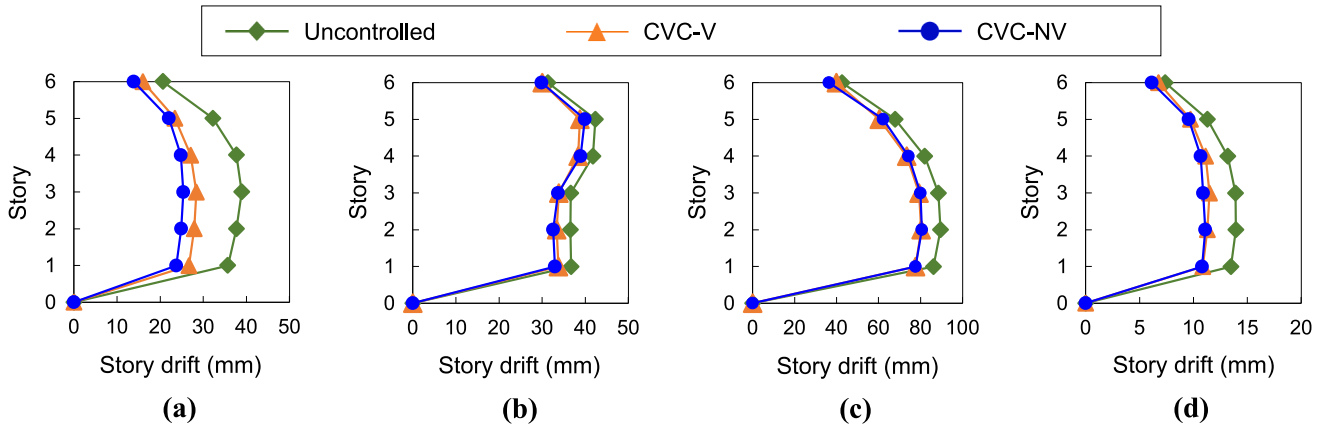

Fig. 28. Peak story drift of the mainframe for Case II obtained from the numerical simulation (averaged for each input group): **(a)** simulated waves (Waves M1–3); **(b)** K-NET Oiwake (EW and NS); **(c)** K-NET Hayakita (EW and NS); and **(d)** K-NET Sapporo (EW and NS).

for both Cases I and II. According to Table 11, a satisfactorily higher mainframe acceleration reduction index for the CVC-NV model ($RA_{\text{CVC-NV,MF}}$) was obtained compared with that of the CVC-V model ($RA_{\text{CVC-V,MF}}$).

3.2.3. Evaluation criteria results

The calculated J_1 and J_2 values for the roof, that is, $i = 6$ in Equations (17) and (18), for the mainframe and subframe of the CVC models for Cases I and II are illustrated in Figs. 31 and 32. Here, J_1 and J_2 of Cases I and II were averaged for each of the three simulated waves and six observed record inputs. The J_1 and J_2 of the mainframe for the CVC-NV and CVC-V models are less than unity, exhibiting a reasonable response

reduction performance achieved in both CVC models, as shown in Fig. 31. Furthermore, the J_1 and J_2 of the mainframe for the CVC-NV model are clearly decreased or roughly comparable to those of the CVC-V model for both Cases I and II. However, the value of J_1 and J_2 of the subframe in the CVC-NV model is not clearly reduced, as presented in Fig. 32.

The promising response control performances for the mainframe of the CVC-NV model discussed in Subsections 3.2.1–3.2.3 were attained with smaller viscous damping coefficient values (c^C) at the connection compared to those of the CVC-V model (Table 8). This was attributed to the negative stiffness applied at the connection in the CVC-NV model. A previous study [18] using one-story CVC systems based on the transfer
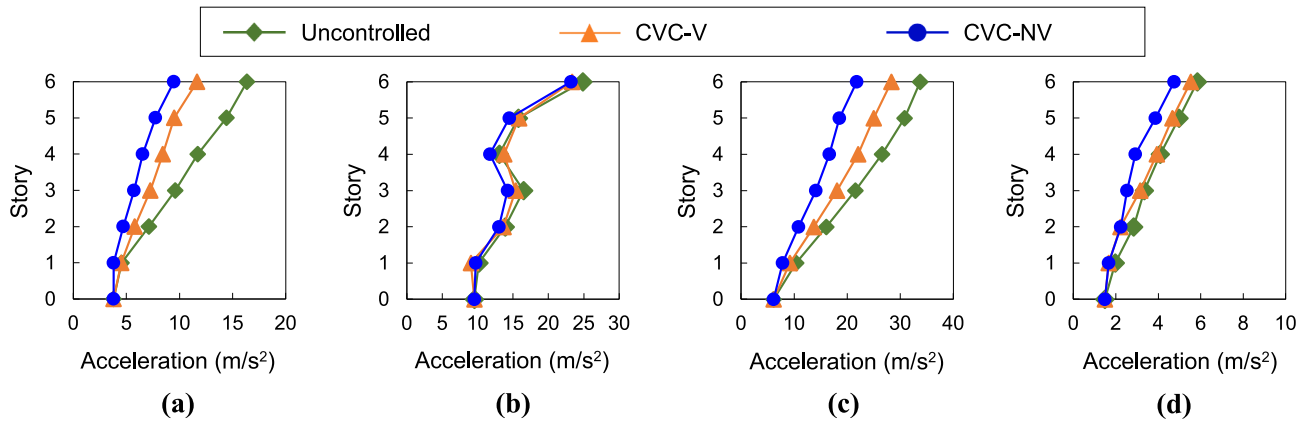
Fig. 29. Peak acceleration of the mainframe for Case I obtained from the numerical simulation (averaged for each input group): **(a)** simulated waves (Waves M1–3); **(b)** K-NET Oiwake (EW and NS); **(c)** K-NET Hayakita (EW and NS); and **(d)** K-NET Sapporo (EW and NS).
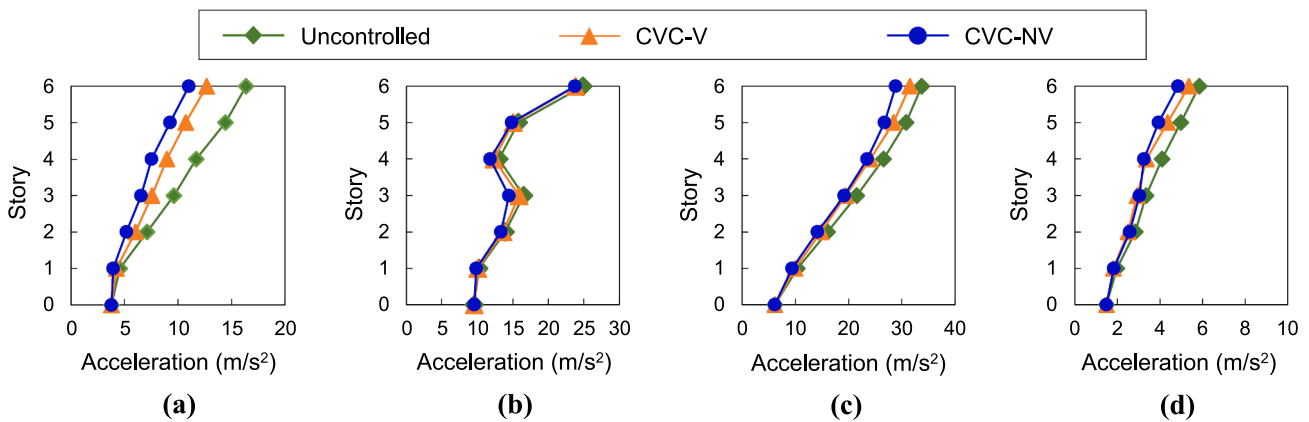

Fig. 30. Peak acceleration of the mainframe for Case II obtained from the numerical simulation (averaged for each input group): **(a)** simulated waves (Waves M1–3); **(b)** K-NET Oiwake (EW and NS); **(c)** K-NET Hayakita (EW and NS); and **(d)** K-NET Sapporo (EW and NS).

Table 10
Displacement reduction indices of the mainframe for the CVC-V and CVC-NV models obtained from the numerical simulation.

Input motion	Case I		Case II	
	Displacement reduction index for CVC-V ($RD_{\text{CVC-V,MF}}$)	Displacement reduction index for CVC-NV ($RD_{\text{CVC-NV,MF}}$)	Displacement reduction index for CVC-V ($RD_{\text{CVC-V,MF}}$)	Displacement reduction index for CVC-NV ($RD_{\text{CVC-NV,MF}}$)
Mean for the three simulated waves	0.465	0.474	0.266	0.341
Mean for the six observed records	0.233	0.270	0.123	0.132

function reported that the optimal viscous damping coefficient required for minimizing the peak amplitude of the displacement transfer function of the mainframe of CVC model with negative stiffness and dashpot was decreased compared to CVC model without negative stiffness (i.e., with only dashpot). The results of the reduced viscous damping in the CVC-NV model obtained from the present simulation using six-story CVC systems roughly correspond to the results reported in the literature [18]. Also, the obtained control performance for the mainframe of the CVC-NV model indicates the potential for effective seismic retrofitting of existing buildings by connecting to a newly built subframe structure using negative stiffness as the connecting element.

Table 11
Acceleration reduction indices of the mainframe for the CVC-V and CVC-NV models obtained from the numerical simulation.

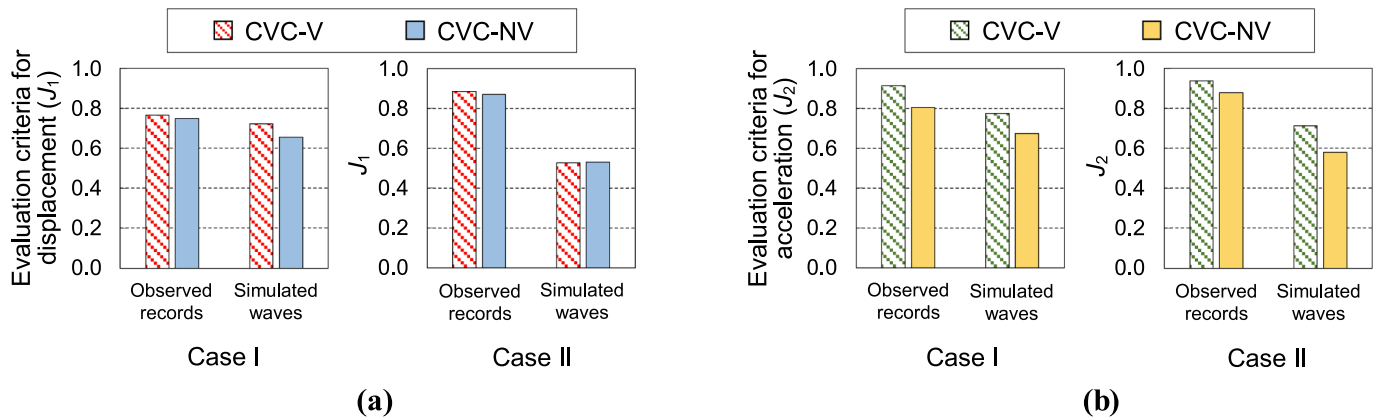| Input motion	Case I		Case II	
	Acceleration reduction index for CVC-V ($RA_{\text{CVC-V,MF}}$)	Acceleration reduction index for CVC-NV ($RA_{\text{CVC-NV,MF}}$)	Acceleration reduction index for CVC-V ($RA_{\text{CVC-V,MF}}$)	Acceleration reduction index for CVC-NV ($RA_{\text{CVC-NV,MF}}$)
Mean for the three simulated waves	0.221	0.370	0.191	0.292
Mean for the six observed records	0.089	0.205	0.077	0.107

Fig. 31. Evaluation criteria at the roof of the mainframe for the controlled models (averaged for each input of the six observed records and three simulated waves): **(a)** peak relative displacement responses (J_1); and **(b)** peak absolute acceleration responses (J_2).
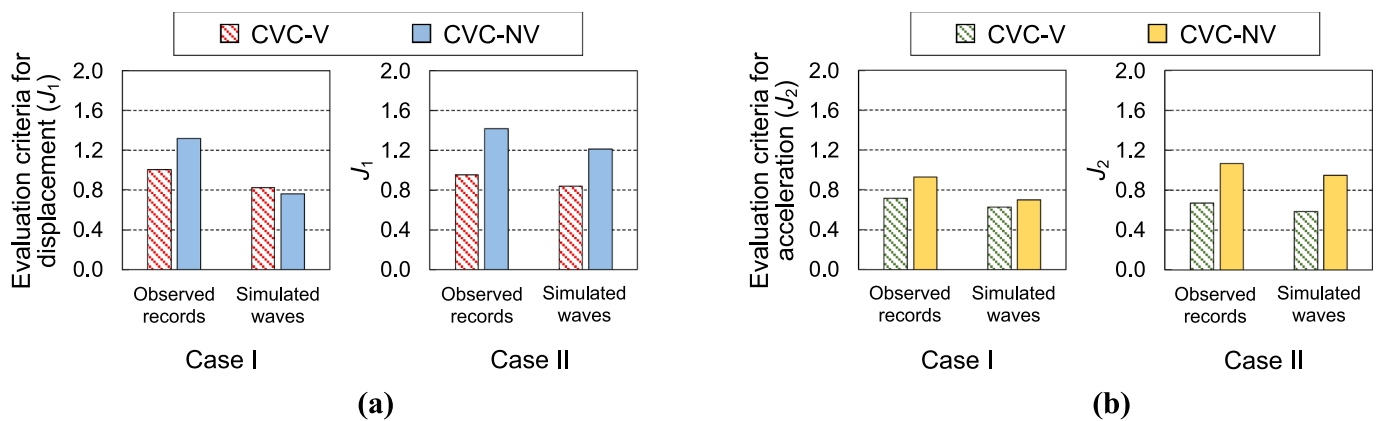

Fig. 32. Evaluation criteria at the roof of the subframe for the controlled models (averaged for each input of the six observed records and three simulated waves): **(a)** peak relative displacement responses (J_1); and **(b)** peak absolute acceleration responses (J_2).

4. Conclusions

This study experimentally and numerically investigated the response behavior and control effects of CVC structural systems with a PNS spring as a connector subjected to dynamic excitations. Shake table experiments were conducted using CVC system specimens incorporating PNSDs consisting of curved-leaf springs. In addition, time-history earthquake response simulations were performed using six-story CVC building models connected by negative stiffness and viscous damping elements. The following conclusions were drawn:

(1) In the shake table experiments, PNSD-1 and PNSD-2 exhibited an initial negative stiffness owing to the pre-compression effect, and the three PNSDs exhibited an increased second negative stiffness owing to the onset of snap-through buckling in the subtracted hysteresis loops of the PNSDs.
(2) An effective response control performance for the mainframe under seismic excitations was attained by incorporating a PNSD as the connector of the CVC specimen.
(3) The CVC specimen with PNSD-2 exhibited the most effective control performance among the three PNSDs for mitigating the response displacement and acceleration under the simulated wave input.
(4) In the numerical simulations, both the CVC-NV and CVC-V models exhibited a reduced mainframe peak response displacement and acceleration compared to that of the uncontrolled model (UC-MF).

(5) The peak response displacement and acceleration of the mainframe of the CVC-NV model clearly decreased or were roughly comparable to those of the CVC-V model. Thus, incorporating negative stiffness and viscous damping connectors into CVC systems is promising for reducing the seismic response.
(6) The CVC-NV model reasonably performed with a smaller viscous damping coefficient value at the connection than that of the CVC-V model because of the negative stiffness incorporated into the CVC-NV model.

Future research tasks include a comparison of the data obtained from the shake table experiments with numerical response simulation results.

CRediT authorship contribution statement

Sonia Longjam: Methodology, Software, Validation, Formal analysis, Investigation, Writing – original draft, Writing – review & editing, Funding acquisition. **Kazutaka Shirai:** Conceptualization, Methodology, Investigation, Writing – original draft, Writing – review & editing, Supervision, Project administration, Funding acquisition.

Declaration of Competing Interest

The authors declare that they have no known competing financial interests or personal relationships that could have appeared to influence the work reported in this paper.

Data availability

Data will be made available on request.

Acknowledgements

References

[1] Zhang WS, Xu YL. Vibration analysis of two buildings linked by Maxwell model-defined fluid dampers. J Sound Vib 2000;233(5):775–96. https://doi.org/10.1006/jsvi.1999.2735.

[2] Kageyama M., Yasui Y., Seto K. The principal solutions of connecting spring and damper for optimum vibration control under several criteria. Journal of Structural and Construction Engineering, AIJ 2000;65(529):97–104. (in Japanese). https://doi.org/10.3130/aijs.65.97.

[3] Ni YQ, Ko JM, Ying ZG. Random seismic response analysis of adjacent buildings coupled with non-linear hysteretic dampers. J Sound Vib 2001;246(3):403–17. https://doi.org/10.1006/jsvi.2001.3679.

[4] Minami S., Yamazaki S., Toyama K., Tahara K. Experimental study on coupled vibration control structures. The 13th World Conference on Earthquake Engineering, 2004;Paper No. 2351, August 1-6. Vancouver, Canada.

[5] Christenson RE, Spencer Jr BF, Johnson EA, Seto K. Coupled building control considering the effects of building/connector configuration. *J Struct Eng*, ASCE 2006;132(6):853–63. https://doi.org/10.1061/(ASCE)0733-9445(2006)132:6 (853).

[6] Cimellaro GP, Lopez-Garcia D. Algorithm for design of controlled motion of adjacent structures. Struct Control Health Monit 2011;18(2):140–8. https://doi.org/10.1002/stc.357.

[7] Basili M, De Angelis M, Fraraccio G. Shaking table experimentation on adjacent structures controlled by passive and semi-active MR dampers. J Sound Vib 2013;332(13):3113–33. https://doi.org/10.1016/j.jsv.2012.12.040.

[8] Palacios-Quiñonero F, Rubió-Massegú J, Rossell JM, Karimi HR,. Vibration control for adjacent structures using local state information. Mechatronics 2014;24(4):336–44. https://doi.org/10.1016/j.mechatronics.2013.08.001.

[9] Jankowski R, Mahmoud S. Linking of adjacent three-storey buildings for mitigation of structural pounding during earthquakes. Bull Earthq Eng 2016;14:3075–97. https://doi.org/10.1007/s10518-016-9946-z.

[10] Basili M, De Angelis M. Vibration analysis and models of adjacent structures controlled by magnetorheological dampers. Shock Vib 2017;9596382. https://doi.org/10.1155/2017/9596382.

[11] Al-Fahdawi OAS, Barroso LR, Soares RW. Simple adaptive control method for mitigating the seismic responses of coupled adjacent buildings considering parameter variations. Eng Struct 2019;186:369–81. https://doi.org/10.1016/j.engstruct.2019.02.025.

[12] Al-Fahdawi OAS, Barroso LR, Soares RW. Semi-active adaptive control for enhancing the seismic performance of nonlinear coupled buildings with smooth hysteretic behavior. Eng Struct 2019;191:536–48. https://doi.org/10.1016/j.engstruct.2019.04.078.

[13] De Domenico D, Qiao H, Wang Q, Zhu Z, Marano G. Optimal design and seismic performance of Multi-Tuned Mass Damper Inerter (MTMDI) applied to adjacent high-rise buildings. Struct Design Tall Spec Build 2020;29(14):e1781. https://doi.org/10.1002/tal.1781.

[14] Kazemi F, Miari M, Jankowski R. Investigating the effects of structural pounding on the seismic performance of adjacent RC and steel MRFs. Bull Earthq Eng 2021;19:317–43. https://doi.org/10.1007/s10518-020-00985-y.

[15] Lu L, Xu J, Zhou Y, Lu W, Spencer Jr BF. Viscous inertial mass damper (VIMD) for seismic responses control of the coupled adjacent buildings. Eng Struct 2021;233:111876. https://doi.org/10.1016/j.engstruct.2021.111876.

[16] Abbaszadeh MA, Hamidi H, Amiri JV. On seismic response reduction of adjacent frame: emphasis on the different characteristics of earthquakes. International Journal of Civil Engineering 2022;20:91–106. https://doi.org/10.1007/s40999-021-00655-3.

[17] Djerouni S, Elias S, Abdeddaim M, Rupakhety R. Optimal design and performance assessment of multiple tuned mass damper inerters to mitigate seismic pounding of adjacent buildings. Journal of Building Engineering 2022;48:103994. https://doi.org/10.1016/j.jobe.2022.103994.

[18] Longjam S, Shirai K. Numerical investigation of earthquake response reduction effects by negative stiffness connection for adjacent building structures. Structures 2022;38:672–88. https://doi.org/10.1016/j.istruc.2022.01.078.

[19] Iemura H, Kouchiyama O, Toyooka A, Shimoda I (2008) Development of the friction-based passive negative stiffness damper and its verification tests using shaking table. *The 14th World Conference on Earthquake Engineering*, October 12−17, 2008, Beijing, China.

[20] Nagarajaiah S, Pasala DTR, Reinhorn A, Constantinou M, Sirilis AA, Taylor D. Adaptive negative stiffness: a new structural modification approach for seismic protection. Adv Mat Res 2013;639−640:54−66. https://doi.org/10.4028/www.scientific.net/AMR.639-640.54.

[21] Sarlis AA, Pasala DTR, Constantinou MC, Reinhorn AM, Nagarajaiah S, Taylor DP. Negative stiffness device for seismic protection of structures. *J Struct Eng*, ASCE 2013;139(7):1124–33. https://doi.org/10.1061/(ASCE)ST.1943-541X.0000616.

[22] Wang M, Sun FF, Nagarajaiah S. Simplified optimal design of MDOF structures with negative stiffness amplifying dampers based on effective damping. Struct Design Tall Spec Build 2019;28(15):e1664. https://doi.org/10.1002/tal.1664.

[23] Shirai K, Noro S, Walsh KK. Shake table testing of a passive negative stiffness device with curved leaf springs for seismic response mitigation of structures. Struct Control Health Monit 2021;28(7):e2736. https://doi.org/10.1002/stc.2736.

[24] Yamada Y, Ikawa N, Yokoyama H, Tachibana E (1994) Active control of structures using the joining member with negative stiffness. *The First World Conference on Structural Control*, TP2, Vol. **2**: 41–49, 1994, California, USA.

[25] Ikawa N, Yamada Y, Yokoyama H, Tachibana E. Active control system of coupled structures with a negative stiffness. J Struct Eng, AIJ 1996;42B:629−34 (in Japanese).

[26] Shimizu K, Kurino H (2009) Fundamental study of structural control with negative stiffness connection. Part 1: Study of applicability of negative stiffness. *Summaries of Technical Papers of Annual Meeting*, AIJ:453−454. **(in Japanese)**.

[27] Kurino H, Shimizu K (2009) Fundamental study of structural control with negative stiffness connection. Part 2: Feasibility study utilizing variable damping device. *Summaries of Technical Papers of Annual Meeting*, AIJ:455−456. **(in Japanese)**.

[28] Longjam S, Shirai K (2021) Use of negative stiffness for coupled vibration control structures: an analytical investigation. *The 17th World Conference on Earthquake Engineering*, September 27−October 2, 2021, Sendai, Japan.

[29] Longjam S (2022) Seismic response of coupled structures using passive negative stiffness connection Ph.D. dissertation, Hokkaido University, Japan.

[30] Shirai K, Inoue N. A seismic response estimation method for RC structures using random vibration theory. J Adv Concr Technol 2014;12(2):62–72. https://doi.org/10.3151/jact.12.62.

[31] National Research Institute for Earth Science and Disaster Resilience, Strong motion Seismograph Networks (K-NET, KiK-net). Accessed 17 April 2020. https://www.kyoshin.bosai.go.jp.

[32] Shirai K, Matsumoto R, Horii J. Questionnaire survey of the occupants of high-rise residential buildings in Sapporo after the 2018 Hokkaido Eastern Iburi Earthquake. Journal of Asian Architecture and Building Engineering 2021;21(3):884–99. https://doi.org/10.1080/13467581.2021.1900856.

[33] Shirai K, Kamada K, Kobayashi K. Damage survey and residual seismic capacity evaluation of reinforced concrete school buildings after the 2018 Hokkaido Eastern Iburi Earthquake. J Earthq Eng 2021;26(13):7032–55. https://doi.org/10.1080/13632469.2021.1961928.

[34] The MathWorks Inc.: MATLAB (R2022a). https://www.mathworks.com.

[35] Ohtori Y, Christenson RE, Spencer Jr BF, Dyke SJ. Benchmark control problems for seismically excited nonlinear buildings. J Eng Mech 2004;130(4):366–85. https://doi.org/10.1061/(ASCE)0733-9399(2004)130:4(366).